J. Fluid Mech. (1998), *vol.* 377, *pp.* 99–136. Printed in the United Kingdom

Stability of plane Couette flow of a granular material

By MEHEBOOB ALAM[1]† AND PRABHU R. NOTT[2]

[1]Department of Mechanical Engineering, and [2]Department of Chemical Engineering,
Indian Institute of Science, Bangalore 560012, India
e-mail: prnott@chemeng.iisc.ernet.in

(Received 25 August 1997 and in revised form 13 July 1998)

This paper presents a linear stability analysis of plane Couette flow of a granular material using a kinetic-theory-based model for the rheology of the medium. The stability analysis, restricted to two-dimensional disturbances, is carried out for three illustrative sets of grain and wall properties which correspond to the walls being perfectly adiabatic, and sources and sinks of fluctuational energy. When the walls are not adiabatic and the Couette gap H is sufficiently large, the base state of steady fully developed flow consists of a slowly deforming 'plug' layer where the bulk density is close to that of maximum packing and a rapidly shearing layer where the bulk density is considerably lower. The plug is adjacent to the wall when the latter acts as a sink of energy and is centred at the symmetry axis when it acts as a source of energy. For each set of properties, stability is determined for a range of H and the mean solids fraction $\bar{\nu}$. For a given value of $\bar{\nu}$, the flow is stable if H is sufficiently small; as H increases it is susceptible to instabilities in the form of cross-stream layering waves with no variation in the flow direction, and stationary and travelling waves with variation in the flow and gradient directions. The layering instability prevails over a substantial range of H and $\bar{\nu}$ for all sets of wall properties. However, it grows far slower than the strong stationary and travelling wave instabilities which become active at larger H. When the walls act as energy sinks, the strong travelling wave instability is absent altogether, and instead there are relatively slow growing long-wave instabilities. For the case of adiabatic walls there is another stationary instability for dilute flows when the grain collisions are quasi-elastic; these modes become stable when grain collisions are perfectly elastic or very inelastic. Instability of all modes is driven by the inelasticity of grain collisions.

1. Introduction

In recent years, observations in experiments and computer simulations of particle segregation, cluster formation and fluctuations in the stress (Hopkins & Louge 1991; Savage 1992*a*; Goldhirsch, Tan & Zanetti 1993; Miller, O'Hern & Behringer 1996) of granular flows have motivated analyses of their stability. The formation of inhomogeneities and clusters is an issue of fundamental importance since it has direct consequences on the rheology of the granular medium. It is, therefore, of interest to determine whether the phenomena of clustering and stress fluctuations are a consequence of instabilities arising in flows and whether they can be explained by the continuum equations of motion.

† Current address: Department of Applied Maths and Engineering Sciences, University of California, San Diego, La Jolla, CA 92093, USA.

In a recent paper, Wang, Jackson & Sundaresan (1996) reported a linear stability analysis of rapid granular shear flow, using a kinetic-theory-based model for the rheology of the medium. They laid to rest some speculations and discrepancies in some earlier studies on the stability of an unbounded uniformly shearing granular medium (Savage 1992*b*; Babić 1993; Schmid & Kytömaa 1994) and proceeded to analyse the stability of a granular material bounded between two impenetrable parallel plates moving relative to each other at a constant speed. They give results for three representative sets of wall properties that correspond to the flux of fluctuational energy from the boundary into the shearing material being exactly zero, positive and negative, i.e. the walls being adiabatic, sources of fluctuational energy and sinks of fluctuational energy, respectively. However, they report that the properties of the walls have little bearing on the nature of instabilities and remark that particle segregation patterns "appear to be remarkably insensitive to the physical properties of the particles and the bounding wall".

This paper also addresses the stability of plane Couette flow of a granular material. Our results indicate that the base states of steady fully developed flow computed by Wang *et al.* (1996) are incorrect when the Couette gap is sufficiently large. The only case for which the base states are given in their paper is when the plates are 89 particle diameters apart and the mean solids fraction is 0.35 (their figure 2); the velocity profiles for two sets of wall properties show only minor deviations from the linear profile, and there is little density variation across the gap. In contrast, our solutions for the same parameter set show profound deviations from the linear velocity profile and the presence of dense non-deforming zones when the walls act as sources or sinks of fluctuational energy. Therefore, it appears that the stability results of Wang *et al.* are based on incorrect computation of the base-state profiles when the walls are non-adiabatic.

In this paper, we show that the nature of instabilities in plane Couette flow of a granular material is more complex than what was reported by Wang *et al.* We observe that the properties of the walls exert considerable influence on the nature of instabilities and on the critical Couette gap for the onset of instability. We show the existence of travelling wave instabilities of the kind observed in the simulations of Hopkins & Louge (1991) and a stationary instability in dilute flows for the case of adiabatic walls, neither of which has been reported earlier.

Since the base state contains dense slowly deforming regions, it would have been appropriate to include the frictional stress arising from abiding grain contacts. This was done in our recent analysis of the stability of unbounded shear of a granular medium (Alam & Nott 1997) using the frictional-kinetic model for the rheology. However, this model has proved problematical when applied to the bounded shear flow of the present study. When there is a dense plug in the flow field, the shear rate within the plug becomes very small; since the frictional stress is indeterminate at zero shear rate, numerical solution was not possible. This difficulty may perhaps be overcome by assuming the existence of a non-deforming plug (within which only the frictional stress acts), with deformation occurring only in a shear layer, as in the work of Mohan, Nott & Rao (1997). We do not address this issue in the present study and consider a purely kinetic stress, therefore making the study valid only for the regime of rapid shear.

2. Governing equations and constitutive relations

We consider a granular material bounded by two solid plane walls at $\tilde{y} = -\tilde{H}/2$ and $\tilde{y} = \tilde{H}/2$. The upper wall moves with a velocity $U_w/2$ in the $\tilde{x}$-direction and the lower wall moves with the same speed in the opposite direction. The granular material

consists of grains of diameter d_p and mass density ρ_p. The velocity components are $\tilde{u}$ and $\tilde{v}$ in the $\tilde{x}$- and $\tilde{y}$-directions respectively, the solids fraction (volume fraction of solids) is denoted by ν and the grain temperature by $\tilde{T}$.

The equations of motion in the absence of gravity are

$$\rho_p \frac{\mathrm{D}\nu}{\mathrm{D}\tilde{t}} = -\rho_p \nu(\tilde{\boldsymbol{\nabla}} \cdot \tilde{\boldsymbol{u}}), \tag{2.1}$$

$$\rho_p \nu \frac{\mathrm{D}\tilde{\boldsymbol{u}}}{\mathrm{D}\tilde{t}} = -\tilde{\boldsymbol{\nabla}} \cdot \tilde{\boldsymbol{\Sigma}}, \tag{2.2}$$

$$\tfrac{3}{2}\rho_p \nu \frac{\mathrm{D}\tilde{T}}{\mathrm{D}\tilde{t}} = -\tilde{\boldsymbol{\nabla}} \cdot \tilde{\boldsymbol{q}} - \tilde{\boldsymbol{\Sigma}} : \tilde{\boldsymbol{\nabla}}\tilde{\boldsymbol{u}} - \tilde{\mathscr{D}}. \tag{2.3}$$

Here $\mathrm{D}/\mathrm{D}\tilde{t}$ is the usual material derivative and $\tilde{\boldsymbol{\Sigma}}$ is the stress tensor. The last of the above equations is a balance for the fluctuational, or 'pseudo-thermal', kinetic energy; here, $\tilde{\boldsymbol{q}}$ is the energy flux, $\tilde{\boldsymbol{\Sigma}} : \tilde{\boldsymbol{\nabla}}\tilde{u}$ the production due to shear work, and $\tilde{\mathscr{D}}$ the dissipation due to inelastic collisions. This balance is required as the transport properties of the granular material depend on the grain temperature $\tilde{T}$.

As indicated earlier, we choose a constitutive model for the stress, energy flux and dissipation rate that is appropriate for *rapid* granular flow. Kinetic-theory-based models for a system of smooth identical inelastic spheres have been derived by Jenkins & Savage (1983), Lun *et al.* (1984), Jenkins & Richman (1985) and subsequently elaborated in a few other studies. Jenkins & Savage (1983) presented the simplest analysis by assuming the singlet velocity distribution to be Maxwellian, but their analysis has the desirable feature of accounting for the anisotropy in the distribution of collisions. More systematic derivations, with the velocity distribution perturbed from the Maxwellian, were presented by Lun *et al.* (1984) and Jenkins & Richman (1985); though their methods were different, the constitutive relations given in these two studies are identical. Later, Jenkins & Richman (1988) determined the anisotropy in the second moment of velocity fluctuations of smooth inelastic circular disks for the particular case of uniform shear; their analysis shows significant normal stress differences for dilute flows, but none in the dense limit. This anisotropy has been shown to arise only in the Burnett-order corrections to the constitutive relations in the recent work of Sela & Goldhirsch (1998).

We use the constitutive relations of Lun *et al.* in this work as they have been widely used in the analysis of rapid granular flows. Moreover, any systematic analysis that stops at terms linear in spatial gradients of the hydrodynamic variables in the perturbation to the velocity distribution function will yield the same constitutive relations (Jenkins & Richman 1988; Sela & Goldhirsch 1998). Hence our analysis is of general import and in no way specific to a particular constitutive model. We do not probe the consequence of anisotropy on stability, for reasons given in the concluding section. We shall demonstrate that the primary features of the constitutive model that determine stability are the dissipative nature of grain collisions, the compressibility of the medium, and the dependence of the transport properties on the grain temperature T. These features are common to all models for rapid granular flows. A point to bear in mind is that all analyses based on kinetic theory assume instantaneous binary collisions and invoke the assumption of molecular chaos. These assumptions are unlikely to hold at high densities, and hence the constitutive model we use is not expected to be valid at solids fractions close to that of maximum packing. We shall nevertheless present results for all densities in this paper for the sake of completeness.

$f_1(v)$	$v(1+4\eta v g(v))$
$f_2(v)$	$\frac{(2+\alpha)}{3\pi^{1/2}}\left(\frac{5\pi}{96\eta(2-\eta)}\left(1+\frac{8}{5}\eta v g(v)\right)\left(\frac{1}{g(v)}+\frac{8}{5}\eta(3\eta-2)v\right)+\frac{8}{5}\eta v^2 g(v)\right)$
$f_3(v)$	$\frac{8}{3\pi^{1/2}}\eta v^2 g(v)$
$f_4(v)$	$\frac{25\pi^{1/2}}{16\eta(41-33\eta)}\left(1+\frac{12}{5}\eta v g(v)\right)\left(\frac{1}{g(v)}+\frac{12}{5}\eta^2(4\eta-3)v\right)+\frac{4}{\pi^{1/2}}\eta v^2 g(v)$
$f_{4h}(v)$	$\frac{25\pi^{1/2}}{16\eta(41-33\eta)}\left(\frac{1}{v g(v)}+\frac{12}{5}\eta\right)\frac{12}{5}\eta(2\eta-1)(\eta-1)\frac{\mathrm{d}}{\mathrm{d}v}(v^2 g(v))$
$f_5(v)$	$\frac{48}{\pi^{1/2}}\eta(1-\eta)v^2 g(v)$
$f_6(v)$	$\frac{\sqrt{3}\pi v g(v)}{2v_{max}f_4(v)}$
$f_7(v)$	$\frac{\pi v g(v)}{2\sqrt{3}v_{max}f_2(v)}$
η	$\frac{1}{2}(1+e_p)$

TABLE 1. Non-dimensional functions

The constitutive expressions of Lun *et al.* (1984) are

$$\tilde{\boldsymbol{\Sigma}} = \rho_p\left(f_1(v)\,\tilde{T} - d_p\,f_3(v)\,\tilde{T}^{1/2}\tilde{\boldsymbol{\nabla}}\cdot\tilde{\boldsymbol{u}}\right)\boldsymbol{I} - 2\,\rho_p\,d_p\,f_2(v)\,\tilde{T}^{1/2}\boldsymbol{S}, \tag{2.4}$$

$$\tilde{\boldsymbol{q}} = -\,\rho_p\,d_p\,f_4(v)\,\tilde{T}^{1/2}\tilde{\boldsymbol{\nabla}}\tilde{T} - \rho_p\,d_p\,f_{4h}(v)\,\tilde{T}^{3/2}\,\tilde{\boldsymbol{\nabla}}v, \tag{2.5}$$

$$\tilde{\mathscr{D}} = \frac{\rho_p}{d_p}f_5(v)\,\tilde{T}^{3/2}, \tag{2.6}$$

where

$$\boldsymbol{S} = \tfrac{1}{2}\left(\tilde{\boldsymbol{\nabla}}\tilde{\boldsymbol{u}} + \tilde{\boldsymbol{\nabla}}\tilde{\boldsymbol{u}}^T\right) - \tfrac{1}{3}\left(\tilde{\boldsymbol{\nabla}}\cdot\tilde{\boldsymbol{u}}\right)\boldsymbol{I},$$

and $\boldsymbol{I}$ is the identity tensor. The non-dimensional functions of the solids fraction, f_1 to f_5 are listed in table 1. Since the analysis of Lun *et al.* is strictly valid only for small grain inelasticity, the parameter η must be set to unity in the functions f_1 to f_{4h}. Wang *et al.* (1996) used the forms given in table 1 and we retain them to aid comparison with their work; the error incurred in doing so is of order $(1-\eta)$ and will therefore have little effect on the qualitative nature of the solutions. The factor $(2+\alpha)/3$ in $f_2(v)$ was not present in the original expression of Lun *et al.* but was introduced later by Johnson & Jackson (1987) (and retained by Wang *et al.*) to reflect the anisotropy of collision distribution. As in these studies, we have set α to 1.6. For the equilibrium radial distribution function at contact, $g(v)$, we use the form

$$g(v) = \frac{1}{1-(v/v_{max})^{1/3}} \tag{2.7}$$

which ensures that $g \to \infty$ when $v \to v_{max}$ and hence constrains the solids fraction to remain less than the maximum packing limit v_{max}, which is taken to be 0.65.

Using the wall-to-wall gap $\tilde{H}$ as the length scale, the velocity difference between the walls U_w as the velocity scale and the inverse of the nominal shear rate $\tilde{H}/U_w$ as

the time scale, we introduce the following non-dimensional variables:

$$\left.\begin{aligned} (x,y) &= \frac{1}{\tilde{H}}(\tilde{x},\tilde{y}), & t &= \frac{U_w}{\tilde{H}}\tilde{t},\\ (u,v) &= \frac{1}{U_w}(\tilde{u},\tilde{v}), & T &= \frac{\tilde{T}}{(d_p/\tilde{H})^2 U_w^2}\\ \boldsymbol{\Sigma} &= \frac{\tilde{\boldsymbol{\Sigma}}}{\rho_p U_w{}^2 (d_p/\tilde{H})^2}, & \boldsymbol{q} &= \frac{\tilde{\boldsymbol{q}}}{\rho_p U_w{}^3 (d_p/\tilde{H})^4},\\ \mathscr{D} &= \frac{\tilde{\mathscr{D}}}{\rho_p U_w{}^3 (d_p/\tilde{H})^3/d_p}. \end{aligned}\right\} \tag{2.8}$$

The non-dimensional equations of motion in terms of dynamical variables v, u, v, and T are then

$$\frac{\partial v}{\partial t} + \frac{\partial}{\partial x}(vu) + \frac{\partial}{\partial y}(vv) = 0, \tag{2.9}$$

$$v\left[\frac{\partial u}{\partial t} + u\frac{\partial u}{\partial x} + v\frac{\partial u}{\partial y}\right] = -\frac{1}{H^2}\frac{\partial p}{\partial x} + \frac{1}{H^2}\frac{\partial}{\partial x}\left[2\mu\frac{\partial u}{\partial x} + \lambda(\nabla\cdot u)\right] + \frac{1}{H^2}\frac{\partial}{\partial y}\left[\mu\left(\frac{\partial u}{\partial y} + \frac{\partial v}{\partial x}\right)\right], \tag{2.10}$$

$$v\left[\frac{\partial v}{\partial t} + u\frac{\partial v}{\partial x} + v\frac{\partial v}{\partial y}\right] = -\frac{1}{H^2}\frac{\partial p}{\partial y} + \frac{1}{H^2}\frac{\partial}{\partial y}\left[2\mu\frac{\partial v}{\partial y} + \lambda(\nabla\cdot u)\right] + \frac{1}{H^2}\frac{\partial}{\partial x}\left[\mu\left(\frac{\partial u}{\partial y} + \frac{\partial v}{\partial x}\right)\right], \tag{2.11}$$

$$\tfrac{3}{2}v\left[\frac{\partial T}{\partial t} + u\frac{\partial T}{\partial x} + v\frac{\partial T}{\partial y}\right] = \frac{1}{H^2}\frac{\partial}{\partial x}\left[\kappa\frac{\partial T}{\partial x} + \kappa_h\frac{\partial v}{\partial x}\right] + \frac{1}{H^2}\frac{\partial}{\partial y}\left[\kappa\frac{\partial T}{\partial y} + \kappa_h\frac{\partial v}{\partial y}\right] - p\left(\frac{\partial u}{\partial x} + \frac{\partial v}{\partial y}\right) + 2\mu\left[\left(\frac{\partial u}{\partial x}\right)^2 + \left(\frac{\partial v}{\partial y}\right)^2 + \tfrac{1}{2}\left(\frac{\partial u}{\partial y} + \frac{\partial v}{\partial x}\right)^2 + \frac{\lambda}{2\mu}\left(\frac{\partial u}{\partial x} + \frac{\partial v}{\partial y}\right)^2\right] - \mathscr{D}, \tag{2.12}$$

where

$$\left.\begin{aligned} p(v,T) &= f_1(v)\,T, & \mu(v,T) &= f_2(v)\,T^{1/2},\\ \lambda(v,T) &= (\zeta - \tfrac{2}{3}\mu), & \zeta(v,T) &= f_3(v)\,T^{1/2},\\ \kappa(v,T) &= f_4(v)\,T^{1/2}, & \kappa_h(v,T) &= f_{4h}(v)\,T^{3/2},\\ \mathscr{D}(v,T) &= f_5(v)\,T^{3/2}. \end{aligned}\right\} \tag{2.13}$$

Here H is the dimensionless wall separation $\tilde{H}/d_p$.

2.1. *Boundary conditions*

Unlike in normal fluids, slip is inevitably observed at rigid boundaries in experiments as well as in computer simulations of granular flows. This results in the generation of pseudo-thermal energy at the boundaries; energy is also lost due to inelastic collisions between the particles and the wall. Depending on their relative magnitudes, the boundary can act either as a source or a sink of pseudo-thermal energy.

Boundary conditions for granular flows have been proposed by Hui *et al.* (1984) and Johnson & Jackson (1987) using a heuristic approach, and by Jenkins & Richman

(1986), Richman (1988), Jenkins (1992) and a number of other studies using a more rigorous approach based on kinetic theory. The latter class of papers characterize the wall properties in a detailed manner, while the former give boundary conditions that depend on only two wall properties, namely the coefficient of restitution for particle–wall collisions e_w and the specularity coefficient ϕ'. We use the boundary conditions of Johnson & Jackson in this work. The boundary conditions of Jenkins & Richman essentially reduce to the same form, with the specularity coefficient given in terms of the details of the wall structure.

We only write down the boundary conditions in dimensionless form here, referring to the original work for an elaboration. The first condition is a statement of equality of the tangential stress in the bulk adjacent to the boundary with the tangential momentum flux due to particle–wall collisions:

$$\boldsymbol{n}\cdot\boldsymbol{\Sigma}\cdot\frac{\boldsymbol{u}_s}{|\boldsymbol{u}_s|}=H\,\frac{\boldsymbol{u}_s}{|\boldsymbol{u}_s|}\cdot\boldsymbol{T}^w, \tag{2.14}$$

where $\boldsymbol{T}^w$ is the aforementioned momentum flux, $\boldsymbol{u}_s$ is the slip velocity and $\boldsymbol{n}$ the unit normal from the wall directed into the particle assembly. The second equates the energy flux normal to the wall to the net production of energy at the wall:

$$\boldsymbol{n}\cdot\boldsymbol{q}=H^3\,\boldsymbol{u}_s\cdot\boldsymbol{T}^w-H\,\mathscr{D}^w. \tag{2.15}$$

The tangential momentum flux $\boldsymbol{T}^w$ and the dissipation rate per unit area $\mathscr{D}^w$ are

$$\boldsymbol{T}^w=\frac{\phi'\sqrt{3}\pi\nu\,T^{1/2}\boldsymbol{u}_s}{6\nu_{max}\left[1-\left(\nu/\nu_{max}\right)^{1/3}\right]}, \tag{2.16}$$

$$\mathscr{D}^w=\frac{\sqrt{3}\pi\nu\,T^{3/2}(1-e_w^2)}{4\nu_{max}\left[1-\left(\nu/\nu_{max}\right)^{1/3}\right]}. \tag{2.17}$$

3. Base state

The base state whose stability we wish to analyse is steady, fully developed plane Couette flow,

$$\nu=\nu^0(y),\quad \boldsymbol{u}=\left[u^0(y),\,0\right],\quad T=T^0(y). \tag{3.1}$$

Here and henceforth, the superscript '0' is used to denote base-state fields. The continuity equation is identically satisfied, and the momentum and energy balances take the form

$$\frac{\mathrm{d}}{\mathrm{d}y}\left(\mu^0\frac{\mathrm{d}u^0}{\mathrm{d}y}\right)=0, \tag{3.2}$$

$$\frac{\mathrm{d}p^0}{\mathrm{d}y}=0, \tag{3.3}$$

$$\frac{1}{H^2}\frac{\mathrm{d}}{\mathrm{d}y}\left(\kappa^0\frac{\mathrm{d}T^0}{\mathrm{d}y}+\kappa_h^0\frac{\mathrm{d}\nu^0}{\mathrm{d}y}\right)+\mu^0\left(\frac{\mathrm{d}u^0}{\mathrm{d}y}\right)^2-\mathscr{D}^0=0. \tag{3.4}$$

The boundary conditions (2.14) and (2.15) now reduce to

$$\frac{\mathrm{d}T^0}{\mathrm{d}y}=-\frac{f_{4h}^0}{f_4^0}T^0\frac{\mathrm{d}\nu^0}{\mathrm{d}y}+f_6^0\left[\tfrac{1}{3}\phi'H^3(u^0-1/2)^2-\tfrac{1}{2}H(1-e_w^2)T^0\right], \tag{3.5}$$

$$\frac{\mathrm{d}u^0}{\mathrm{d}y} = -\phi' H f_7^0 (u^0 - 1/2) \tag{3.6}$$

at $y = 1/2$ and

$$\frac{\mathrm{d}T^0}{\mathrm{d}y} = -\frac{f_{4h}^0}{f_4^0} T^0 \frac{\mathrm{d}v^0}{\mathrm{d}y} - f_6^0 \left[\tfrac{1}{3}\phi' H^3 (u^0 + 1/2)^2 - \tfrac{1}{2} H (1 - e_w^2) T^0\right], \tag{3.7}$$

$$\frac{\mathrm{d}u^0}{\mathrm{d}y} = \phi' H f_7^0 (u^0 + 1/2) \tag{3.8}$$

at $y = -1/2$. The non-dimensional functions f_6 and f_7 are listed in table 1. Here and henceforth, f_i^0 refers to the function f_i evaluated at a solids fraction of v^0.

Equations (3.2)–(3.4) along with boundary conditions (3.5)–(3.8) admit the following symmetry:

$$v^0(y) = v^0(-y), \quad u^0(y) = -u^0(-y), \quad T^0(y) = T^0(-y). \tag{3.9}$$

Hence, the solution can be obtained by solving (3.2)–(3.4) in the half-domain $y \in (0, 1/2)$. The relevant boundary conditions at $y = 0$ then are

$$u^0 = 0 \quad \text{and} \quad \frac{\mathrm{d}T^0}{\mathrm{d}y} = 0. \tag{3.10}$$

We emphasize here that the above symmetry need not be obeyed by all the solutions of equations (3.2)–(3.4). Indeed, there are *asymmetric* solutions, which are simply steady states of some of the layering instabilities arising from the base states that we analyse. These asymmetric solutions and other symmetric solutions that arise in plane Couette flow are discussed in detail in a forthcoming paper by Nott *et al.* (1998). They show that all segregated solutions in the adiabatic case arise from layering instabilities of the uniform shear solution (see below), and that these solutions in turn are closely related to the solutions of the source and sink cases.

The solution of the governing equations requires the specification of a boundary condition in addition to (3.5), (3.6) and (3.10). One choice is to specify the normal stress p^0, which is constant across the Couette gap. We have chosen, instead, to impose the integral constraint

$$\overline{v} = \int_{-1/2}^{1/2} v^0(y)\mathrm{d}y \tag{3.11}$$

to specify the mean solids fraction $\overline{v}$ and obtain p^0 as part of the solution.

If the no-slip condition ($u^0(1/2) = 1/2$) is imposed at the wall in place of (3.6), and if e_w is set to unity, the solution of the above set of equations is that of uniform shear:

$$\left.\begin{array}{rcl} v^0(y) & = & \text{constant}\,, \\ u^0(y) & = & y, \\ T^0(y) & = & f_2(v^0)/f_5(v^0). \end{array}\right\} \tag{3.12}$$

Wang *et al.* have referred to this as the adiabatic case, as there is no energy flux normal to the walls; pseudo-thermal energy is not produced because there is no slip and it is not dissipated because grain–wall collisions are perfectly elastic. While this is an idealization of the conditions at the boundaries, we consider it in order to delineate the effects of wall properties on stability.

For the general case of slip at the wall, (3.2)–(3.8) have been solved numerically.

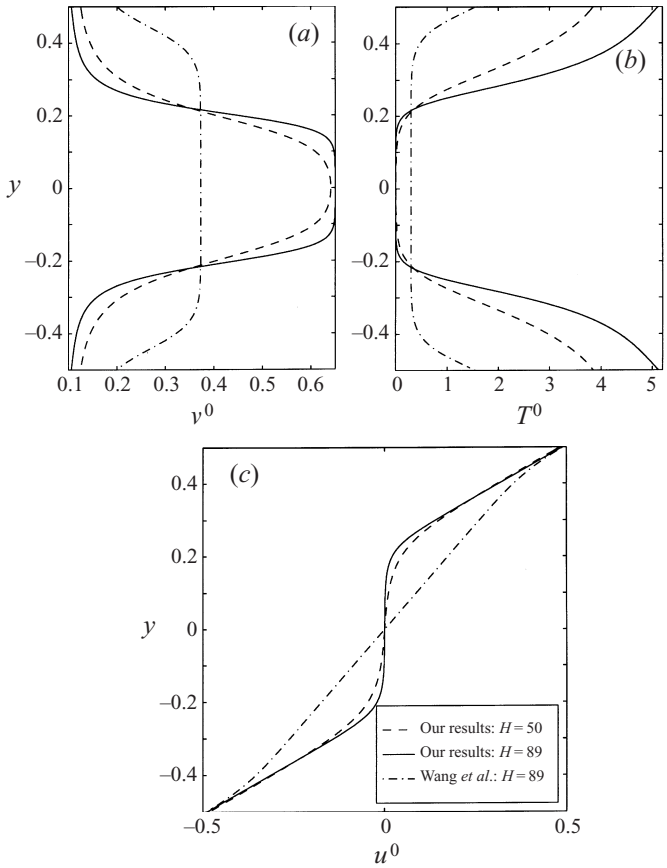

FIGURE 1. Base-state profiles for steady fully developed flow with source walls. Parameter values are $\bar{v} = 0.35$, $e_p = 0.80$ and $e_w = 0.97$. The solid and dashed lines are our results and the dot-dash lines are the results of Wang *et al.* (1996). Note the dense plug at the centre in our solution for $H = 89$.

3.1. *Numerical method and results*

A fourth-order Runge–Kutta marching scheme was used to obtain the solution for the base state; two other numerical schemes, namely a second-order finite difference method and a spectral collocation method, were also used to ascertain the correctness of the solutions. (We were unable to implement the numerical scheme of Wang *et al.* as the details of their linearization procedure are not documented.) Identical results were obtained with all three methods. Our computational procedure for the Runge–Kutta method has been documented by Alam (1998). For a given set of parameters e_p, e_w and ϕ', solutions were obtained for a range of the flow parameters $\bar{v}$ and H by using a numerical continuation procedure. The stability of these base states was analysed subsequently. We note that the system of equations (3.2)–(3.4) is stiff for large H because of the factor H^{-2} multiplying the highest derivative in (3.4).

The values of material parameters used in this study are $e_p = 0.80$ and $\phi' = 0.6$, which were the choices of Wang *et al.* As in their work, we consider stability for three values of e_w, corresponding to the walls being adiabatic ($e_w = 1$, no-slip), and sources ($e_w = 0.97$) and sinks ($e_w = 0.5$) of pseudo-thermal energy.

Figure 1 shows the profiles of v^0, T^0 and u^0 with $e_w = 0.97$ and the average solids fraction, $\bar{v}$, set to 0.35. For comparison, we have superimposed the base-state

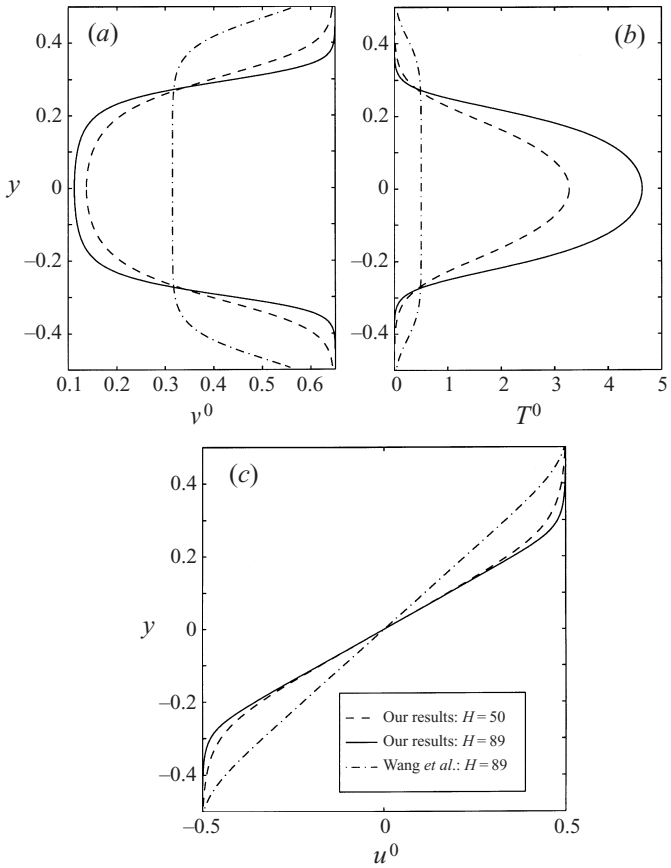

FIGURE 2. Base-state profiles for sink walls, $e_w = 0.50$. Other parameters as in figure 1. Note the dense plugs adjacent to the walls in our solution for $H = 89$.

profiles of Wang *et al.* on each panel (we are grateful to them for providing us with their computed results), represented by the dot-dash lines. It is clear that the grain temperature is maximum at the walls, indicating that the walls supply pseudo-thermal energy to the bulk. Since the pressure across the gap must remain constant, the bulk density is minimum near the walls and maximum at the symmetry axis. Increasing the Couette gap results in a rise in the density at the symmetry axis, and at $H = 89$ there is in fact a dense plug at the centre, where the density is almost that of maximum packing and the shear rate is almost zero. The material is shearing almost uniformly on either side of the plug. The scenario is reversed if e_w is changed to 0.5, as shown in figure 2. Here energy flows from the bulk material to the walls, leaving the walls as sinks of energy. Consequently the plugs are now near the walls, and the sheared layer is at the centre. It is important to note the contrast between our results and those of Wang *et al.*; their solutions show relatively minor deviation from the state of uniform shear, with segregation occurring only in the boundary layers near the walls. Our conclusion that the base states of Wang *et al.* are incorrect for the case of non-adiabatic walls was confirmed by S. Sundaresan & K. Agrawal (private communication, 1997).

If H is sufficiently small, the whole layer shears almost uniformly with only slight variation in v^0 across the gap. This is because the diffusion length for the transport

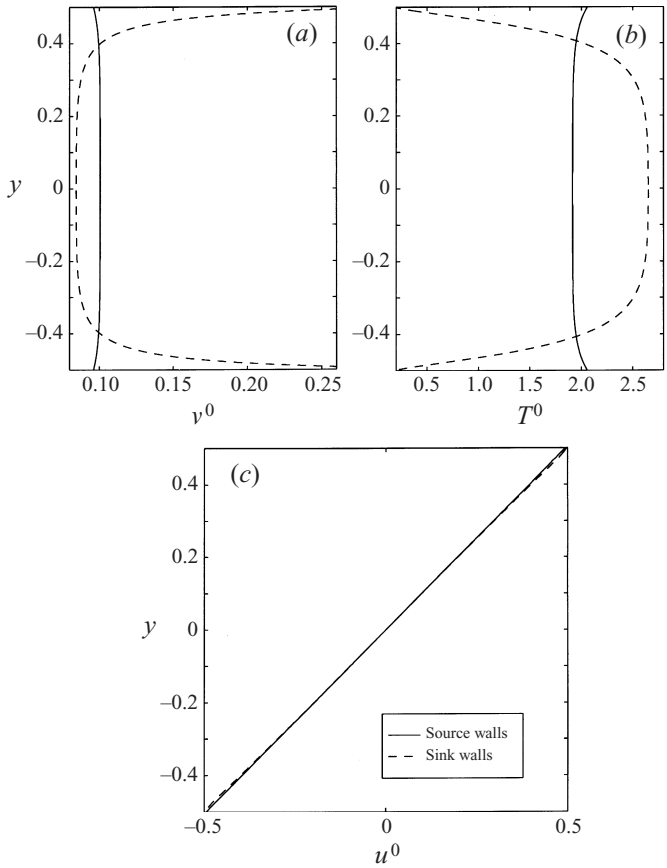

FIGURE 3. Base-state profiles for source and sink walls at $\overline{\nu} = 0.10$, $H = 100$ and $e_p = 0.80$. The velocity profiles are almost linear and the variation in solids fraction across the gap is mild in comparison with figures 1 and 2.

of pseudo-thermal energy varies as the grain diameter d_p. Therefore it increases as a proportion of the Couette gap as H decreases; this has the effect of equalizing the grain temperature, and consequently the density, across the gap. As the mean solids fraction decreases, the regime of approximately uniform shear extends to a larger value of H. This is apparent from figure 3, which shows the profiles of v^0, T^0 and u^0 for a mean solids fraction of 0.1 and a Couette gap of 100. The solid and dashed lines represent results for walls that are sources and sinks of pseudo-thermal energy, respectively. In either case, the effect of the walls extends only to the narrow boundary layers. The thickness of the boundary layer decreases with further rise in H.

It should be clear from the above discussion that there is no analogue of the uniform shear solution for the cases of source and sink walls, except when the flow is dilute. The base-state solutions of the latter are composed of dense zones which suffer little deformation, and relatively dilute shearing zones. The evolution of the solution branches from the 'perfect' case of adiabatic walls to the 'imperfect' case of non-adiabatic walls and a discussion on the nature of the bifurcations for these cases is the subject of a forthcoming paper by Nott *et al.* (1998). The imperfection, in the parlance of bifurcation theory, arises from the boundary conditions: the flux of pseudo-thermal energy vanishes at the walls and at the centreline for the case of

adiabatic walls and hence there are solutions that display symmetry (in v and T) about the planes $y = \pm 1/2$. This symmetry is broken when the walls are not adiabatic.

As mentioned in § 1, we were unable to compute base-state solutions for large H when the frictional-kinetic model (Johnson & Jackson 1987) for the stress was used. Specifically, the angle that specifies the directions of the principal frictional stresses is non-analytic at zero shear rate. Hence numerical solution was not possible when a dense plug is present, as the shear rate becomes arbitrarily small within the plug. We were however able to obtain solutions for H small enough that dense plugs were absent in the flow field.

4. Linear stability analysis

We investigate the stability of steady, fully developed plane Couette flow using the classical normal mode analysis (Drazin & Reid 1981). The base flow is perturbed by infinitesimal disturbances, and their time evolution is studied by linearizing the governing equations about the base state. The perturbations are decomposed into different Fourier modes and because of the linearity of the governing equations, each mode may be analysed separately for stability.

4.1. *Linearized disturbance equations and boundary conditions*

Each of the flow variables is decomposed into its base state and perturbation components,

$$\left.\begin{array}{lllllll} u(x,y,t) & = & u^0(y) + u'(x,y,t), & \qquad v(x,y,t) & = & v'(x,y,t), \\ v(x,y,t) & = & v^0(y) + v'(x,y,t), & \qquad T(x,y,t) & = & T^0(y) + T'(x,y,t). \end{array}\right\} \tag{4.1}$$

We have only considered perturbations in the x- and y-directions in this study, but extending it to three dimensions is straightforward. In this context, it is important to note that Squire's theorem does not hold for rapid granular flows; in other words, we cannot assert that two-dimensional disturbances become unstable sooner than three-dimensional disturbances as any one of the parameters is varied. Substituting (4.1) into the equations of motion (2.9)–(2.12) and linearizing about the base state, we obtain a set of linear equations for the disturbance variables v', u', v', and T'. In operator form, the linearized disturbance equations and boundary conditions may be written as

$$\left.\begin{array}{lcll} \dfrac{\partial X}{\partial t} & = & \mathscr{L}X, & \\ \mathscr{B}_1 X & = & 0 \quad \text{at} & y = 1/2, \\ \mathscr{B}_2 X & = & 0 \quad \text{at} & y = -1/2, \end{array}\right\} \tag{4.2}$$

where $X = (v', u', v', T')^T$ is the disturbance vector. The explicit forms of $\mathscr{L}$ and the boundary operators $\mathscr{B}_1$ and $\mathscr{B}_2$ are given in the Appendix. Note that the coefficients of the linear operator $\mathscr{L}$ depend on the base-state variables (v^0, u^0, T^0) and their spatial derivatives.

The above set of linearized equations and boundary conditions (4.2) do not depend on t explicitly, and are therefore amenable to normal mode analysis. We seek solutions for the solids fraction, velocity and temperature perturbations of the form

$$X(x,y,t) = \hat{X}(y)\, \mathrm{e}^{\mathrm{i}k_x x + \omega t}, \tag{4.3}$$

where $\hat{X}(y)$ are complex functions of y and k_x is the streamwise wavenumber. We have restricted this study to analysing temporal stability, for which k_x is assumed to

be real and ω is complex. The rate of growth or decay of disturbances is determined by ω_r, the real part of ω, and the imaginary part is the frequency. The flow is stable, neutrally stable, or unstable accordingly as ω_r is negative, equal to zero, or positive, respectively.

Before proceeding to discuss the solution of the linearized equations, it is useful to consider the symmetries in the solution. It follows immediately from the symmetry of the base-state solution (3.9) that (4.2) is invariant under the transformation

$$x \to -x, \quad y \to -y, \quad \omega \to \omega, \quad [\hat{v}, \hat{u}, \hat{v}, \hat{T}] \to [\hat{v}, -\hat{u}, -\hat{v}, \hat{T}]. \tag{4.4}$$

This implies that if $e^{ik_x x}[\hat{v}, \hat{u}, \hat{v}, \hat{T}](y)$ is an eigenmode of the stability equations with eigenvalue ω, then so is $e^{-ik_x x}[\hat{v}, -\hat{u}, -\hat{v}, \hat{T}](-y)$. This is simply an invariance to rotation of the coordinate frame as there is no preferential direction (such as gravity) in the problem. Thus, for every forward propagating mode there is a backward propagating mode with the same growth rate.

4.2. *Numerical method for stability analysis*

The above set of linearized disturbance equations along with boundary conditions constitute a well-posed boundary value problem. However, a straightforward discretization results in a system of equations requiring two artificial boundary conditions for the perturbation in solids fraction (Malik 1990). One can use the momentum balance in the direction normal to the walls as the artificial boundary conditions at the boundaries. While this method was successful in computing the spectra for plane Couette flow of a compressible Newtonian fluid (details in Alam 1998), for the present problem it always yielded a spurious eigenvalue which did not converge when the number of collocation points was increased.

The ambiguity inherent in identifying the spurious mode may be avoided altogether by employing a staggered grid spectral collocation scheme in which the continuity equation is collocated at points lying between the collocation points for the energy and momentum equations, and therefore not at the boundaries (Canuto *et al.* 1988; Malik 1990). This is accomplished by representing the solids fraction by a polynomial one degree lower than that for the velocity and grain temperature. At the same time a set of interpolating matrices must be formed to interpolate between the two grids. This method does not result in spurious eigenvalues as the spectrum converges satisfactorily when the number of collocation points is increased. This is the approach taken in this work, the details of which are documented in Alam (1998).

The momentum and energy balances are collocated at the N Gauss–Lobatto points, which are the extrema of the Chebyshev polynomial of degree N, and the continuity equation at its $(N-1)$ zeros. When the discretized stability equations, along with the boundary conditions are formulated as a matrix eigenvalue problem, they take the form

$$\boldsymbol{A}\Phi = \omega \boldsymbol{B}\Phi \tag{4.5}$$

where ω is the eigenvalue and Φ is the discrete representation of the eigenfunction; $\boldsymbol{A}$ and $\boldsymbol{B}$ are square matrices of order $(4N+3)$. Since the boundary conditions do not contain the eigenvalue ω, $\boldsymbol{B}$ is singular. This singularity is removed through row and column operations and the order of the matrices reduced to $(4N-3)$. The eigenvalues of the generalized eigenvalue problem (4.5) are determined with the aid of a complex QR-algorithm (Golub & van-Loan 1989) which is available in the MATLAB software package. All the computations reported here were performed on an IBM RS/6000 workstation.

The accuracy of the numerical scheme was ascertained by increasing the number of collocation points N until the leading eigenvalues converged to values independent of N. For the case of adiabatic walls it was found that 20 points are sufficient for $k_x = 0$ when the Couette gap H is less than 200. For larger values of H, more points are needed to achieve convergence. When the walls are sources or sinks of energy, the presence of dense plugs makes the matrix eigenvalue problem ill-conditioned and hence more collocation points were required to accurately compute the eigenvalues. In general we find that the larger the value of $k_x H$, the larger is the number of collocation points required to achieve convergence. A great deal of care was taken to ensure accurate computation of the eigenvalues. The accuracy and validity of the numerical scheme was ensured by favourable comparison with analytical results for a limiting case, as we shall show in § 5, and also with published results for the following stability problems: (i) incompressible Couette flow (Gallagher & Mercer 1962); (ii) compressible Couette flow (Duck, Erlebacher & Hussaini 1994); (iii) granular Couette flow of Wang *et al.*

Out of $(4N - 3)$ eigenvalues of (4.5), the one with maximum ω_r at a given k_x is referred to as the leading eigenvalue, and the supremum of all leading modes (i.e. maximum of ω_r over all k_x) as the *dominant* eigenvalue. For a given set of material and wall properties, there are two other flow parameters, H and $\overline{\nu}$. We shall display the stability results by plotting contours of the dominant eigenvalue in the $(H, \overline{\nu})$-plane.

Due to the profound differences between the base-state profiles we have computed and those of Wang *et al.*, we find that our stability results also differ considerably from theirs. They report that the properties of the walls have little bearing on the nature of instabilities. In contrast, we observe that the properties of the walls exert considerable influence on the nature of instabilities and on the critical Couette gap for the onset of instability. We shall therefore describe in separate sections stability for the three sets of wall properties for which base-state solutions have been determined.

5. Adiabatic walls: uniform shear case

We first consider the case of layering disturbances, i.e. disturbances with $k_x = 0$, as the solution can be obtained analytically. As we shall see further on, a substantial portion of the unstable region in the $(H, \overline{\nu})$-plane is due to layering modes. The importance of layering modes in unbounded and bounded shear flows was underlined earlier by Wang *et al.* We also note that layering structures have been observed by Tan (1995) in his simulations of plane Couette flow of smooth inelastic disks.

The linear disturbance equations (A 1)–(A 5) with $k_x = 0$ reduce to

$$\omega\hat{v} + v^0 \frac{\mathrm{d}\hat{v}}{\mathrm{d}y} = 0, \tag{5.1}$$

$$v^0 H^2 \left[\omega\hat{u} + u_y^0 \hat{v}\right] = u_y^0 \mu_v^0 \frac{\mathrm{d}\hat{v}}{\mathrm{d}y} + \mu^0 \frac{\mathrm{d}^2\hat{u}}{\mathrm{d}y^2} + u_y^0 \mu_T^0 \frac{\mathrm{d}\hat{T}}{\mathrm{d}y}, \tag{5.2}$$

$$v^0 H^2 \omega\hat{v} = -p_v^0 \frac{\mathrm{d}\hat{v}}{\mathrm{d}y} + \left(2\mu^0 + \lambda^0\right) \frac{\mathrm{d}^2\hat{v}}{\mathrm{d}y^2} - p_T^0 \frac{\mathrm{d}\hat{T}}{\mathrm{d}y}, \tag{5.3}$$

$$\begin{aligned} \tfrac{3}{2} v^0 \omega \hat{T} = {} & \frac{1}{H^2}\left[\kappa_h^0 \frac{\mathrm{d}^2}{\mathrm{d}y^2} + H^2\left(\mu_v^0 u_y^{0\,2} - \mathscr{D}_v^0\right)\right]\hat{v} \\ & + 2u_y^0 \mu^0 \frac{\mathrm{d}\hat{u}}{\mathrm{d}y} - p^0 \frac{\mathrm{d}\hat{v}}{\mathrm{d}y} + \frac{1}{H^2}\left[\kappa^0 \frac{\mathrm{d}^2}{\mathrm{d}y^2} + H^2\left(\mu_T^0 u_y^{0\,2} - \mathscr{D}_T^0\right)\right]\hat{T} \end{aligned} \tag{5.4}$$

and the boundary conditions to

$$\hat{u} = \hat{v} = \frac{\mathrm{d}\hat{T}}{\mathrm{d}y} = 0 \tag{5.5}$$

at $y = \pm 1/2$. Equations (5.1)–(5.4) along with boundary conditions (5.5) admit the following symmetry relationships:

$$\left.\begin{array}{lllllll} \hat{v}(y) & = & \hat{v}(-y), & \hat{T}(y) & = & \hat{T}(-y), \\ \hat{u}(y) & = & -\hat{u}(-y), & \hat{v}(y) & = & -\hat{v}(-y) \end{array}\right\} \tag{5.6}$$

and

$$\left.\begin{array}{lllllll} \hat{v}(y) & = & -\hat{v}(-y), & \hat{T}(y) & = & -\hat{T}(-y), \\ \hat{u}(y) & = & \hat{u}(-y), & \hat{v}(y) & = & \hat{v}(-y). \end{array}\right\} \tag{5.7}$$

It can then be easily verified that the solution for the disturbance variables is

$$\left.\begin{array}{lllllll} \hat{v}(y) & = & \hat{v}_1 \cos k_n(y \pm 1/2), & \hat{T}(y) & = & \hat{T}_1 \cos k_n(y \pm 1/2), \\ \hat{u}(y) & = & \hat{u}_1 \sin k_n(y \pm 1/2), & \hat{v}(y) & = & \hat{v}_1 \sin k_n(y \pm 1/2), \end{array}\right\} \tag{5.8}$$

where $k_n = n\pi$, the mode number n being a positive integer. The even modes correspond to the first symmetry group (5.6) and the odd modes correspond to the second (5.7). Note that $n = 0$ is a trivial mode representing a uniform disturbance.

Substituting (5.8) into (5.1)–(5.4), we obtain an eigenvalue problem, whose dispersion relation may be readily obtained as

$$\omega^4 + a_3\omega^3 + a_2\omega^2 + a_1\omega + a_0 = 0. \tag{5.9}$$

The coefficients a_0–a_3 are real, the expressions for which are too cumbersome to reproduce here but may be found in Alam (1998). Hence, we have three possibilities for the roots: all real, two complex conjugate pairs, or two real and one complex conjugate pair. In the limit of large H, an asymptotic analysis (Alam 1998) indicates that there are two real roots and a complex conjugate pair; our computations reveal this to be the case for all H. One of the real roots represents the least-stable mode and thus, as in the case of unbounded granular shear (Alam & Nott 1997), the *principle of exchange of stabilities* (Drazin & Reid 1981, p. 12) holds for bounded shear. Therefore, the locus of neutral stability is given by $a_0 = 0$, which may be simplified to yield

$$H^2 = \frac{N_1}{N_2} k_n^2, \tag{5.10}$$

where

$$N_1 = \frac{1}{f_5^0}\left(f_4^0 - \frac{f_1^0}{f_{1v}^0} f_{4h}^0\right) \quad \text{and} \quad N_2 = \left(\frac{f_{5v}^0}{f_5^0} + \frac{f_{2v}^0}{f_2^0}\right)\frac{f_1^0}{f_{1v}^0} - 2.$$

It is clear from (5.10) that higher the mode number n, larger is the critical value of H for the onset of its instability; therefore the $n = 1$ mode is the first to become unstable as H increases at a fixed $\bar{\nu}$, and the onset of its instability represents the neutral stability contour in the $(H, \bar{\nu})$-plane, shown in figure 4 by the thin solid line marked '0'. One contour of positive growth rate is also shown in figure 4, obtained by solving (5.9) for ω and taking the maximum of ω_r over all values of n. We observe that the flow is stable to layering modes when the wall separation is sufficiently small; as H exceeds a critical value H_c, which is a function of $\bar{\nu}$, the flow becomes unstable. The flow is always stable to layering modes when $\bar{\nu} < 0.15$.

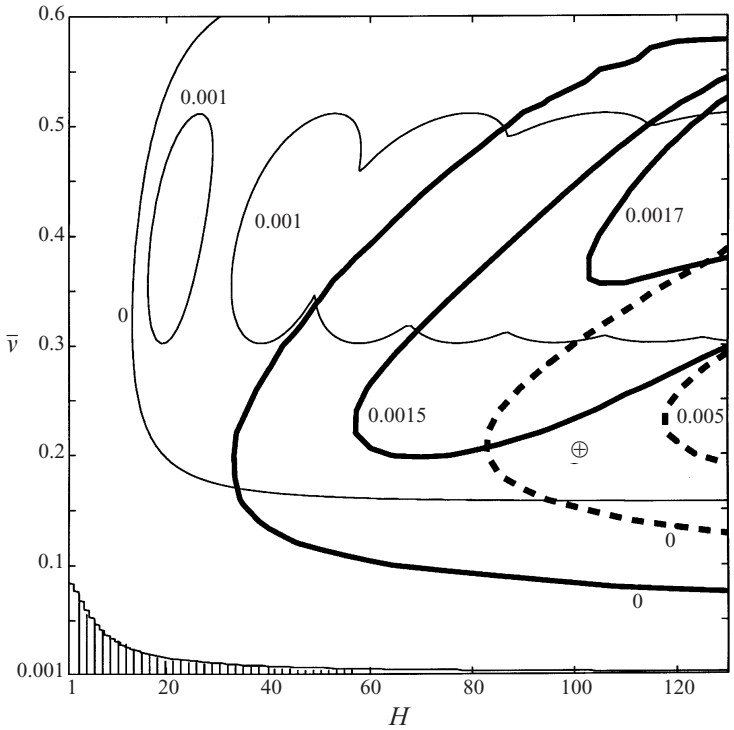

FIGURE 4. The stability map in the $(H, \bar{\nu})$-plane for the adiabatic case with $e_p = 0.80$. The numbers against the contours are the growth rates. The thin solid contours represent layering modes ($k_x = 0$) and the thick solid and dashed contours represent stationary and travelling waves, respectively. The hatched area is a zone of instability for dilute flows.

The contours of constant growth rate for layering modes in figure 4 form sharp cusps, which can be understood if we consider the variation of the growth rates of individual modes with H, shown in figure 5. The circles are the results of our spectral collocation scheme (with 20 collocation points) and the solid lines are the solution of (5.9); eigenvalues obtained from both methods agree to better than eight decimal places, substantiating the accuracy of our numerical computation. For every mode, the growth rate starts with a negative value, increases with H, reaches a maximum positive value and thereafter decays to zero. At some values of H, adjacent modes cross each other, beyond which the higher-order mode becomes dominant until the next crossover. Since $\omega_i = 0$ for all layering modes, the crossovers imply degeneracy in the spectrum. (As we shall see later, degeneracy is also present for non-layering disturbances for all the sets of wall properties considered in this study.) The cusps in the growth rate contours of layering modes in figure 4 are a result of the transfer of dominance from one mode to the next. Note that the growth rate of all modes decreases as H becomes very large. This may be explained if we consider the limit $H \to \infty$, for which the dispersion relation may be further simplified to yield

$$\omega^3 \left(\omega + \frac{2}{3\nu^0} f_5^0 T^{0\,1/2} \right) = 0. \tag{5.11}$$

Three roots of (5.11) are identically zero and the fourth is real and negative. Therefore, every layering mode (with the exception of $n = 0$) becomes neutrally stable in the limit $H \to \infty$.

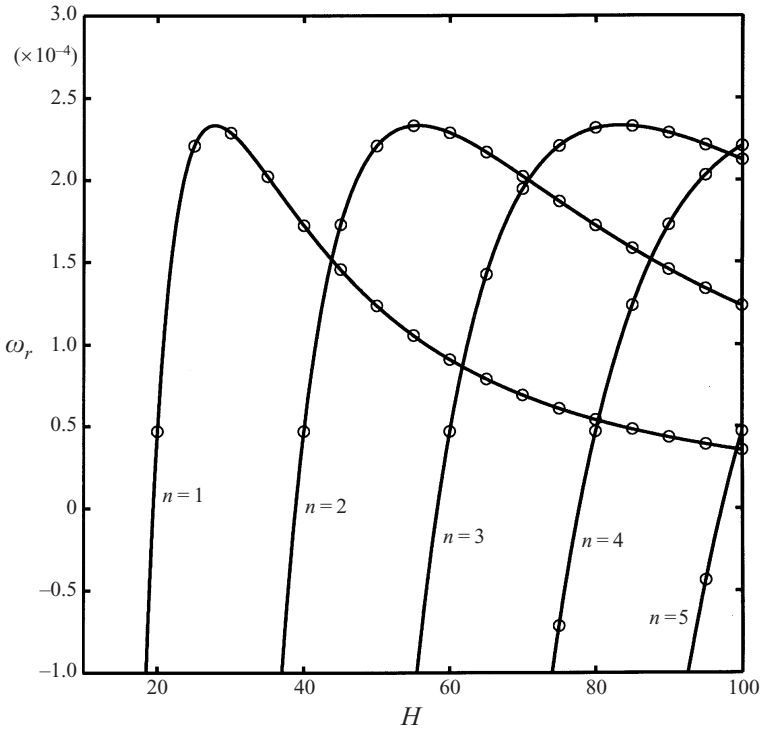

FIGURE 5. Variation of the growth rate of individual layering modes ($k_x = 0$) with H at $\overline{\nu} = 0.20$. Other parameters are as in figure 4.

The Couette gap below which the flow is stable to layering disturbances for all $\overline{\nu}$ (i.e. the minimum of H_c over all $\overline{\nu}$) can be obtained from (5.10) by setting $\partial H/\partial \overline{\nu}$ to zero, which may be simplified to yield

$$\frac{1}{N_1}\left(\frac{\mathrm{d}N_1}{\mathrm{d}\nu^0}\right) - \frac{1}{N_2}\left(\frac{\mathrm{d}N_2}{\mathrm{d}\nu^0}\right) = 0. \tag{5.12}$$

This yields the critical solids fraction $\overline{\nu}_c$ and the critical wall separation H_c may then be calculated from (5.10). For $e_p = 0.80$, we obtain $H_c = 13.27$ and $\overline{\nu}_c = 0.3211$ while $e_p = 0.99$ gives $H_c = 78.07$ and $\overline{\nu}_c = 0.3195$. Note that $\overline{\nu}_c$ is a weak function of e_p due to the weak dependence of (5.12) on e_p; the critical Couette gap is, however, a strong function of e_p, $H_c \sim (1-e_p^2)^{-1/2}$. It is also noteworthy that as $e_p \to 1$, $H_c \to \infty$. In other words, the critical wall separation becomes unbounded in this limit, clearly illustrating the inelastic nature of the instability. Thus, layering instability is driven by the inelasticity of grain collisions, as is the case for unbounded shear flow (Alam & Nott 1997).

It is clear from figure 4 that the flow is stable to layering modes in the dilute limit. This is easily shown by determining the minima of the neutral stability contour, i.e. by setting $\partial \overline{\nu}/\partial H = 0$. This is equivalent to setting N_2 to zero, which is at $\overline{\nu} \approx 0.156$ when $e_p = 0.8$; this does not vary appreciably with e_p due to the weak dependence of N_2 on e_p. Thus the flow is stable to layering disturbances when the mean solids fraction is below 0.156.

Coming to the relation between the unstable modes of bounded and unbounded Couette flow, for a given H all layering modes of the bounded case are compatible

with those of the unbounded case. The unbounded case may be recovered exactly in the limit $H \to \infty$ such that $k_n/H = k_y$. The transverse wavenumber k_y (scaled by the particle diameter) can now take any value, unlike the discrete modes in bounded flow. Therefore, the neutral stability contour for unbounded granular shear flow is given by

$$k_y^2 = \frac{N_2}{N_1} \tag{5.13}$$

in the (ν^0, k_y)-plane.

5.1. *Numerical results for all wavenumbers*

The complete stability diagram for layering ($k_x = 0$) and non-layering ($k_x \neq 0$) disturbances is shown in figure 4 for the case of adiabatic walls, for a particle coefficient of restitution of 0.80. Shown in the figure are contours of constant growth rate; the thin solid contours represent layering modes and the thick solid and dashed contours represent stationary and travelling waves, respectively. The hatched area in the lower left-hand corner of figure 4 represents an additional instability in the dilute limit ($\bar{\nu} \to 0$), which we discuss in § 5.1.1. As in the case of layering disturbances, the flow is also stable to stationary and travelling waves when the gap width H is small; the value of H at which stationary or travelling wave instabilities begin to appear is considerably larger than that for layering instability. Note also that below the minimum $\bar{\nu}$ (≈ 0.156) for layering instability, the flow can become unstable to non-layering disturbances. The neutral stability contour for small $\bar{\nu}$ is determined by disturbances in the form of stationary waves; it is almost horizontal with increasing H, suggesting that this stationary instability is not present as $\bar{\nu} \to 0$. Travelling wave instabilities begin to appear at larger H than layering or stationary instabilities and therefore do not determine the neutral stability contour. In regions of the $(H, \bar{\nu})$-plane where all three modes are unstable, stationary modes have the largest growth rate, followed by travelling and layering modes respectively.

To consider the modal structure in some detail we focus on the point $(H, \bar{\nu}) = (100, 0.20)$ in figure 4, indicated by the symbol $\oplus$, where the flow is unstable to layering, stationary and travelling wave disturbances. At this point, the variation of the growth rate of the leading mode with k_x is shown by the solid line in figure 6(*a*) and that of the phase velocity, defined as

$$c_{ph} = -\frac{\omega_i}{k_x},$$

is shown by the dashed line; a positive c_{ph} indicates a forward propagating wave and a negative c_{ph} a backward propagating wave. The leading mode with a positive growth rate in the long-wave limit (see inset in figure 6*a*) falls rapidly with increasing k_x and soon becomes stable. At larger k_x, two distinct hills protrude above the zero growth rate axis. The first represents the dominant instability due to stationary waves which Wang *et al.* reported; the abrupt change in c_{ph} on either side of this hill indicates transition between travelling and stationary waves. At even smaller wavelengths is the second hill, characterized by a non-zero phase velocity. We note that the dominant travelling wave instability has a growth rate smaller than that of the stationary wave but much larger than that of the long-wave instabilities.

The origin of unstable travelling waves can be traced if we consider the variation of the first few eigenvalues with k_x, shown in figure 6(*b*). The oval structures labelled SW_1 and SW_2 are stationary waves that arise when a complex conjugate pair of eigenvalues becomes purely real. The eigenvalues remain real for a range of k_x, then coalesce again

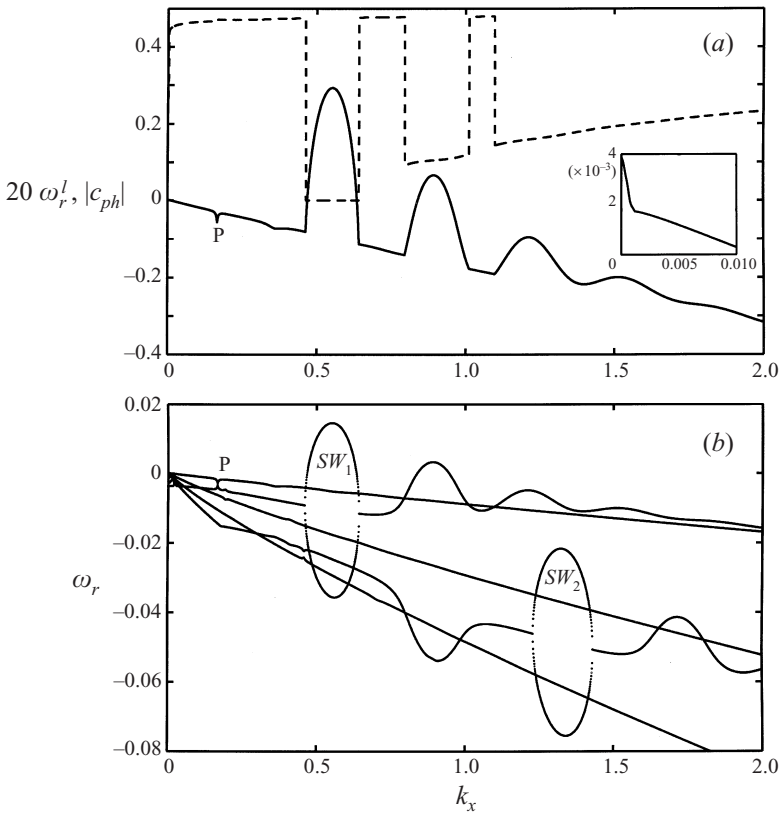

FIGURE 6. (*a*) Variation of the growth rate of the leading mode, ω_r^l, (solid line) and its phase velocity, c_{ph}, (dashed line) with k_x. The inset shows the long-wave variation of ω_r^l. (*b*) Variation of the growth rate of the first few modes with k_x. Parameter values are $H = 100$, $\bar{v} = 0.20$ and $e_p = 0.80$.

to form a complex conjugate pair with further rise in k_x. Indeed we can observe several such instances of stationary waves arising out of travelling waves if we follow the eigenvalues over a larger range of k_x. While only the first stationary mode is unstable for the parameter set considered here, as H increases the other stationary modes SW_2, SW_3 etc. rise and subsequently become unstable. It is clear that the unstable travelling wave arises from the dominant stationary wave in the sense that the two stationary waves of SW_1 coalesce to form two oppositely propagating travelling waves which are unstable for a range of k_x, beyond which they propagate as stable modes. These travelling waves were not reported by Wang *et al.*; for example, the adiabatic case of their figure 17 ($\bar{v} = 0.24$, $H = 89$) should have shown a second hill representing unstable travelling waves at $k_x \approx 1$, as is evident from figure 4 here. The 'kink', in the growth rate of the leading mode, indicated by the letter P in the figures, is a result of crossing of modes. For some values of the mean density (such as $\bar{v} \approx 0.182$), the crossover is a degeneracy as the imaginary parts of the eigenvalues are also equal. In this regard, the points in figure 6(*b*) where travelling waves coalesce to form the stationary waves and vice versa are also where the spectrum is degenerate. Degeneracy in the eigenvalue spectra leads to short-time disturbance growth ($\sim t\mathrm{e}^{\omega t}$), providing a viable mechanism for transition even if the flow is asymptotically stable. It is a common phenomenon in hydrodynamic stability (Craik 1985); for example, plane Couette flow of a Newtonian fluid supports stable degenerate modes (Gustavsson & Hultgren 1980).

To establish the link between layering and non-layering instabilities, we have magnified the region near $k_x = 0$ of figure 6(*b*) and shown in figure 7 the variation of the first few eigenvalues with k_x. Those that start as oscillatory layering modes at $k_x = 0$ are labelled S_1, S_2 etc.; the others start as non-oscillatory layering modes. The inset in figure 7(*a*) shows that the first five modes at $k_x = 0$ are unstable and that there is a neutrally stable mode c_2, which is the $n = 0$ mode of (5.8) representing a uniform disturbance. Comparison with figure 5 shows that the modes a_1, a_2, b_1, b_2 and c_1 correspond to $n = 4,\ 3,\ 2,\ 5$ and 1, respectively, in (5.8). The modes a_1 and a_2 are non-oscillatory ($\omega_i = 0$) at $k_x = 0$, and remain so until they coalesce at $k_x \approx 0.00002$ to form a complex conjugate pair a_{12} representing travelling waves. Similarly, other non-oscillatory modes also coalesce as they evolve with k_x. The mode S_1 originates from the first pair of oscillatory modes, i.e. $n = 1$ of (5.9), and S_2 originates from the $n = 2$ mode. We note in figure 7(*b*) that the phase velocity of these modes diverges as $k_x \to 0$; they resemble some inviscid modes of compressible Couette flows (cf. figure 8 of Duck *et al.* 1994). Further continuation in k_x shows that S_1 splits into two stationary waves at $k_x \approx 0.47$, the first oval structure (SW_1) of figure 6(*b*). The second oval structure (SW_2) of figure 6(*b*) bifurcates from the S_2-branch.

The above discussion clearly establishes the link between the non-layering and layering instabilities. The *non-oscillatory* layering modes always pair up to form travelling waves at small k_x, which may be unstable depending on the values of $\bar{v}$ and H. On the other hand, every pair of *oscillatory* layering modes evolves with k_x initially as travelling waves, and eventually transforms into two stationary waves; with further increase in k_x they pair up again to form travelling waves. More importantly, it is the first pair of oscillatory layering modes (S_1) that evolves with k_x to yield the dominant stationary wave and travelling wave instabilities of figure 4. Thus, though the oscillatory layering modes are always stable, they are the progenitors of the dominant non-layering instabilities.

We now proceed to look at the eigenfunctions of the unstable disturbances. For this, we consider two modes of figure 6(*a*): the dominant stationary wave and the dominant travelling wave. Figure 8(*a*) shows the disturbance in the solids fraction for the dominant stationary wave on a grey scale, with black representing maximum density and white minimum density; contours of constant solids fraction are superimposed on the same figure. Note that the x-coordinate has been scaled by twice the streamwise wavelength. The eigenfunction closely resembles the stationary mode eigenfunction of Wang *et al.* (see their figure 13), since the dominant stationary mode we observe is precisely what they have reported. Figure 8(*b*) shows the disturbance in the solids fraction for the dominant travelling wave. It is interesting to note that the phase velocity of this mode is 0.105; thus the clusters near the walls convect considerably slower than the local mean flow. Here we should recall that there are other travelling instabilities for the same parameter set (see inset of figure 7*a*), although of much higher wavelengths than the one shown in figure 8(*b*).

The description of the modal behaviour thus far has been confined to a single point ($\oplus$) in the (H, $\bar{v}$)-plane. To look at the effect of changing H, we have shown some contours of constant ω_r in the (H, k_x)-plane in figure 9 with $\bar{v} = 0.30$. The line emerging from near the origin, labelled 'LW', is the neutral stability contour for long waves ($k_x \ll 1$), below which is the unstable zone for these modes. The curved sickle-like structures labelled SW, TW_1 etc. are boundaries of the zones of instability for stationary and travelling waves. In a plot such as in figure 6(*a*), these zones are the 'hills' protruding above the $\omega_r = 0$ line. When the Couette gap is large, there is a contiguous range of k_x within which the instability passes on from

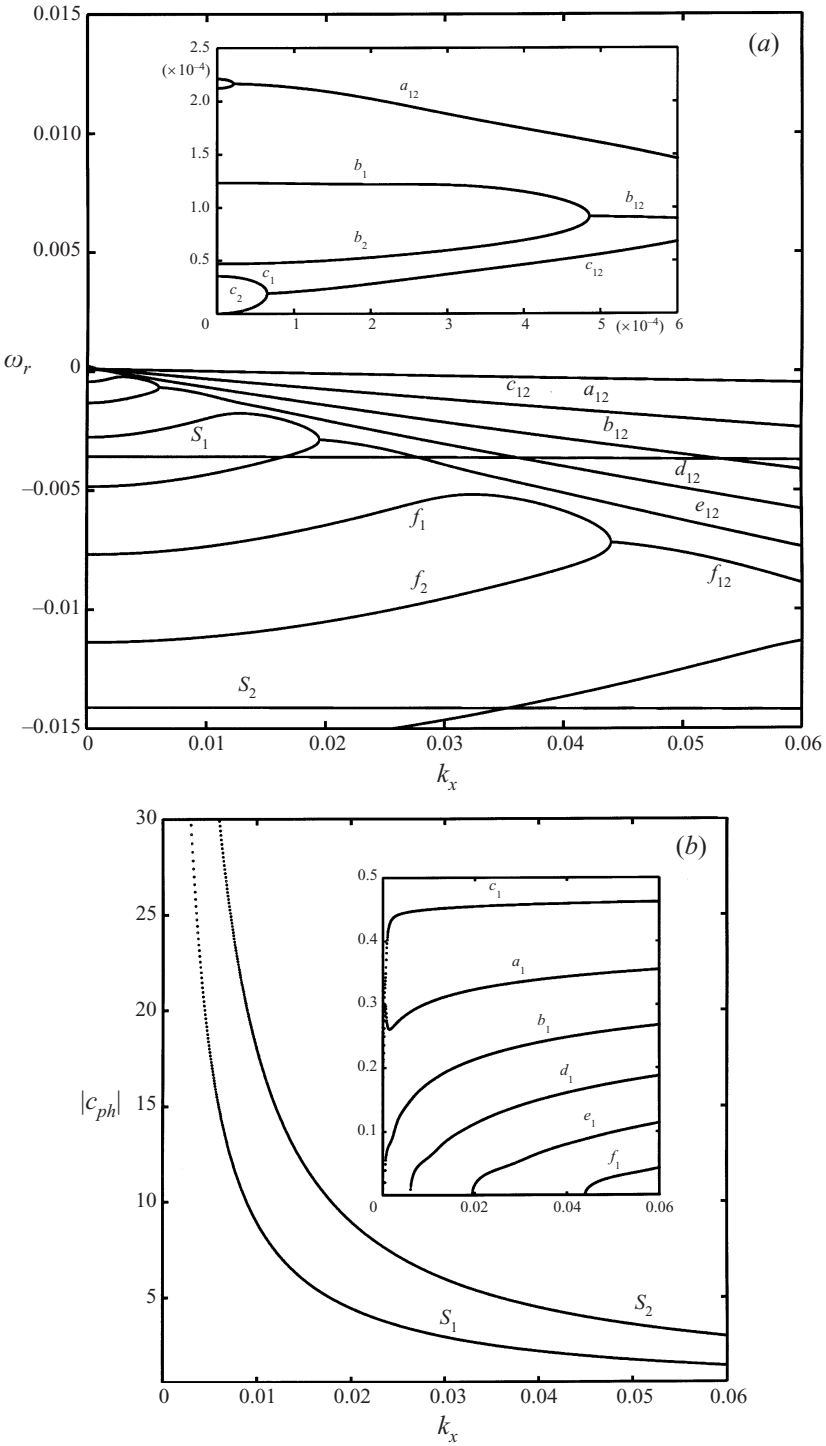

FIGURE 7. The evolution of first few eigenvalues with k_x. The growth rates are shown in (*a*) and the phase velocities in (*b*). Parameter values as in figure 6.

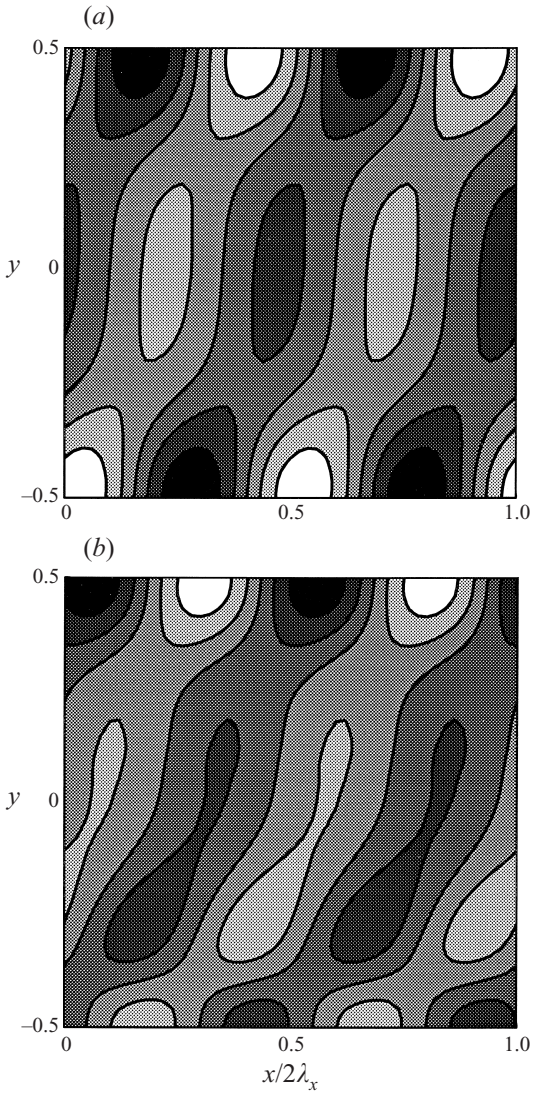

FIGURE 8. The disturbance in the solids fraction for (*a*) the dominant stationary wave and (*b*) the dominant travelling wave of figure 6(*a*). The patterns in (*a*) and (*b*) should be stretched by factors of 23 and 14, respectively, in the *x*-direction to view the true aspect of the clusters.

layering to stationary to travelling waves. For the mean density assumed here, the dominant travelling wave instability, labelled TW_1 in the figure, appears only when the dimensionless gap is more than 100 and the stationary wave appears when it is more than 48. Inspecting the contour values, we find that the growth rate of the dominant travelling wave increases with H, reaches a maximum at some value of H, and thereafter decays. The growth rate of the dominant stationary mode also shows a similar dependence on H.

We find that the effect of e_p on the non-layering instabilities is similar to that on layering instabilities (details in Alam 1998). Decreasing e_p (i.e. increasing grain inelasticity) enhances the growth rate of all instabilities, barring those in the dilute limit (see below). Decreasing e_p also reduces the critical value of H for the inception

of stationary and travelling wave instabilities, i.e. the zone of instability in the $(H, \bar{v})$-plane increases in size with increasing grain inelasticity. Thus, all the observed instabilities are driven by the inelastic nature of particle collisions.

5.1.1. *The dilute limit ($\bar{v} \to 0$)*

We now describe in some detail the instabilities we have observed for dilute flows, corresponding to the hatched area in figure 4. They appear to be strongest in the quasi-elastic limit $1 - e_p \ll 1$, but are absent when collisions are perfectly elastic. An expanded view of the unstable zone in the lower left-hand corner of figure 4 is shown in figure 10. The flow is unstable to the left of the neutral stability contour. The range of H for which the flow is unstable decreases with rise in $\bar{v}$. The range of unstable H (at a given $\bar{v}$) increases as e_p rises from 0.8 to 0.99. The phase velocity of these instabilities is always zero, indicating that they are stationary waves.

Figure 11(a) shows the variation of ω_r^l with wavenumber for four values of e_p at $(H, \bar{v}) = (50, 0.01)$. It is clear that this instability originates as a neutral mode at $k_x = 0$, specifically the mode corresponding to $n = 0$ of (5.8) representing a uniform disturbance. While the leading mode is always stable when $e_p = 0.80$, there is a range of k_x for which it is unstable when e_p is set to 0.99; in this range the growth rate increases with k_x, reaches a maximum at an intermediate value k_x^d, and thereafter decreases monotonically. Further increase in e_p does not change the overall shape of the growth rate curve, but the peak decreases sharply and so does k_x^d. The peak of each curve in figure 11(a) is the dominant eigenvalue, whose variation with e_p is shown in figure 11(b) for the same parameter set. The dashed line in the figure shows the variation of k_x^d. We note that the flow is stable for e_p below 0.88 and unstable when it exceeds this value; ω^d reaches a maximum at $e_p \approx 0.98$ and diminishes with further rise in e_p. The fact that k_x^d also approaches zero in the elastic limit suggests that the dominant mode tends to a neutrally stable layering mode in the perfectly elastic limit. That this instability is absent for e_p below 0.88 contrasts with the instabilities described in § 5.1, which become stronger with increasing grain inelasticity.

The eigenfunction for the solids fraction of the dominant mode is shown in figure 12 on a grey scale for $\bar{v} = 0.01$, $H = 50$ and $e_p = 0.99$; the streamwise wavenumber for this disturbance is 0.22. Note that this is a stationary pattern. Here, as in figure 8, the x-axis should be stretched by a factor of $4\pi/k_x$ to view the true aspect of the disturbance. It appears that the alternating bands of high and low concentrations are aligned almost perpendicular to the direction of the flow.

6. Walls acting as energy sources

We recall that the base state for this case has a dense non-deforming zone around the mid-plane when the Couette gap is sufficiently large. As the Couette gap H increases, the solids fraction in the plug approaches that of maximum packing. This leads to the matrix $\boldsymbol{B}$ in (4.5) becoming increasingly ill-conditioned and requires a large number of collocation points for accurate computation of the eigenvalues, therefore demanding more computational time. This is the reason for the limited range of H for which stability results are given in this section. The considerable difference in the base state from that for adiabatic boundaries leads to stability characteristics that differ significantly from the adiabatic case. We find that the flow becomes stable to layering disturbances if H is sufficiently large, but remains unstable to long-wave disturbances. The strong stationary wave instabilities that were prominent in the adiabatic case are absent here when $\bar{v}$ exceeds a threshold of roughly 0.22; instead, there is a travelling wave insta-

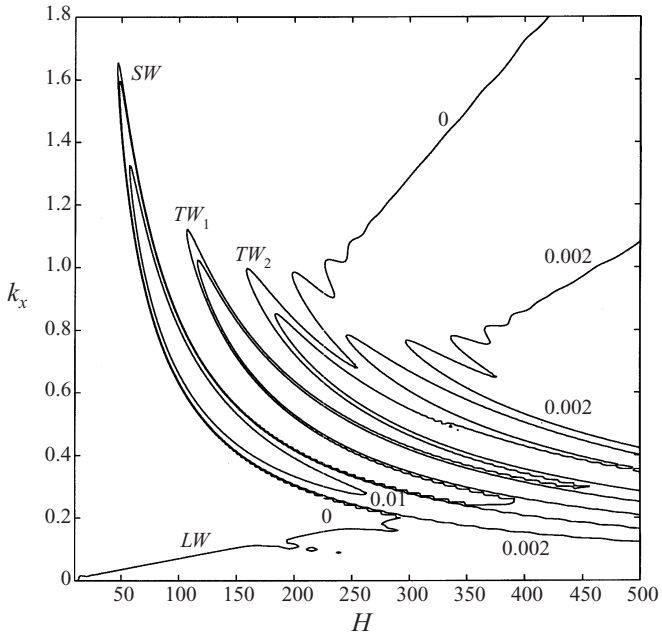

FIGURE 9. Contours of ω_r^l in the (H, k_x)-plane for $\bar{\nu} = 0.30$. Other parameters as in figure 4. The labels LW, SW and TW denote long-wave, stationary wave and travelling wave instabilities respectively.

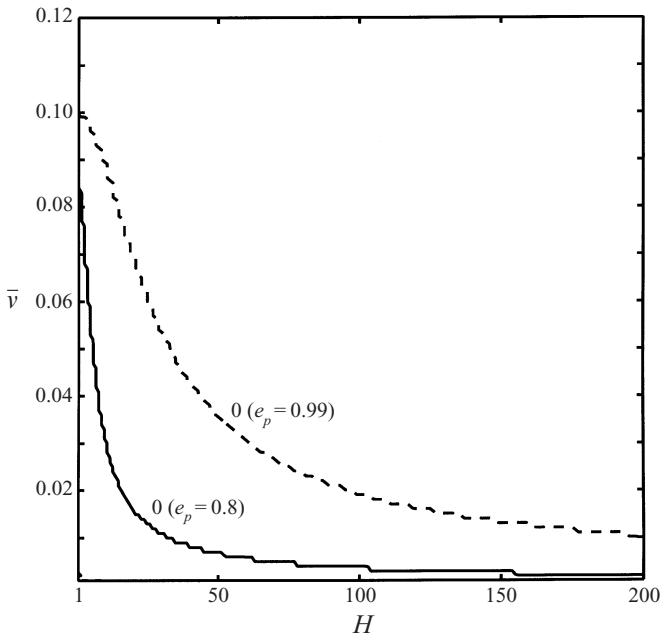

FIGURE 10. Stability map for dilute flows for different e_p. The flow is unstable to the left of the neutral stability contours.

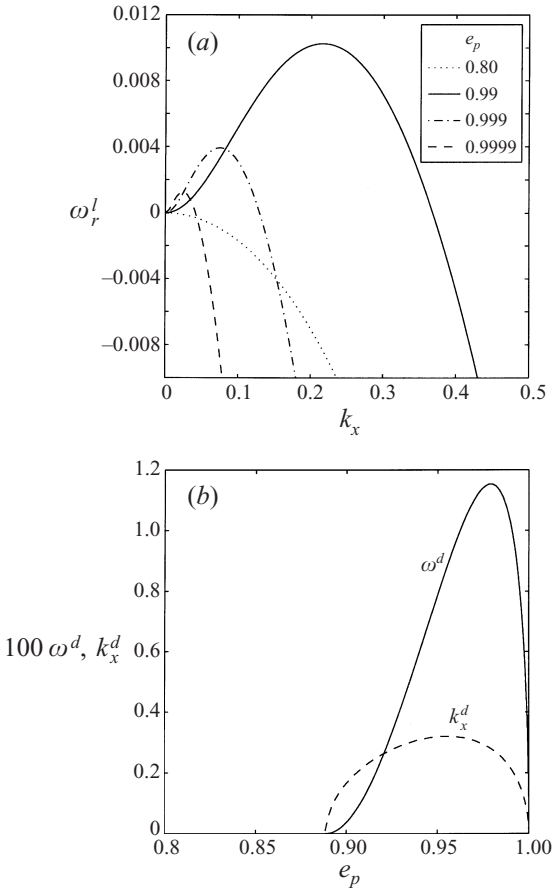

FIGURE 11. (*a*) The growth rate of the leading mode, ω_r^l, as a function of k_x for four values of e_p at $H = 50$ and $\bar{v} = 0.01$. (*b*) The growth rate of the dominant mode and the associated wavenumber (the maxima of the curves in *a*) as a function of e_p.

bility which is the dominant mode at moderate values of $\bar{v}$ and large H. The presence of a plug in the base state also modifies the eigenfunctions of the leading modes.

Before going into the stability map on the $(H, \bar{v})$-plane, it is useful to consider the variation of the leading mode with k_x at a representative point on the plane. Figure 13 shows the variation with k_x of the growth rate and the phase velocity of the leading mode for $(H, \bar{v}) = (50,\ 0.30)$. The inset gives the variation in the long-wave limit. There are two 'hills' rising above the baseline of zero growth rate and one that stays in the stable half-plane. In the first hill, ω_r^l starts off positive at $k_x = 0$ and becomes negative within a k_x of 0.02; the modes in this range of k_x are henceforth referred to as long-wave modes. From the phase velocities in figure 13, it is clear that they are stationary waves. The dominant mode is at the maximum of the second hill, in the form of a travelling wave. The modes in the last hill are also travelling waves, but remain stable for this parameter set. The discontinuities in the phase velocity in figure 13 reflect mode switching, or transfer of dominance from one eigenvalue to another.

Having described the variation of the leading mode with k_x for one particular point in the $(H, \bar{v})$-plane, it is worthwhile to point out qualitative changes in the features

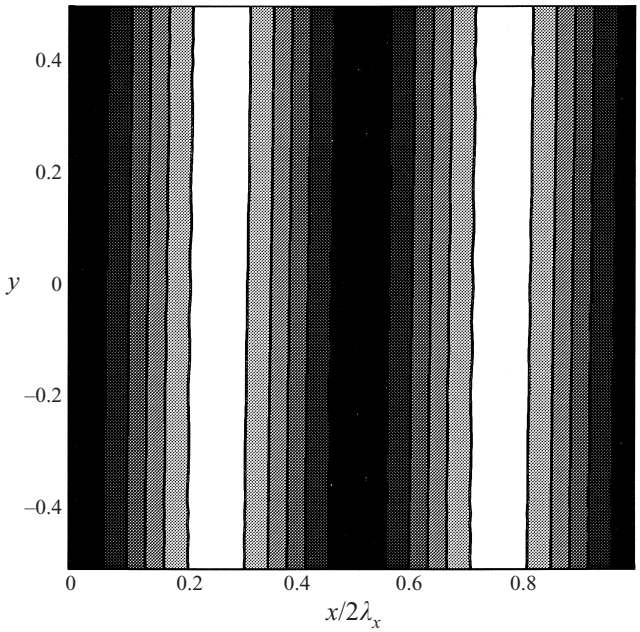

FIGURE 12. The solids fraction disturbance of the dominant mode for $\overline{\nu} = 0.01$, $H = 50$, $e_p = 0.99$. This figure should be stretched by a factor of 57 in the x-direction to view the true aspect the disturbance.

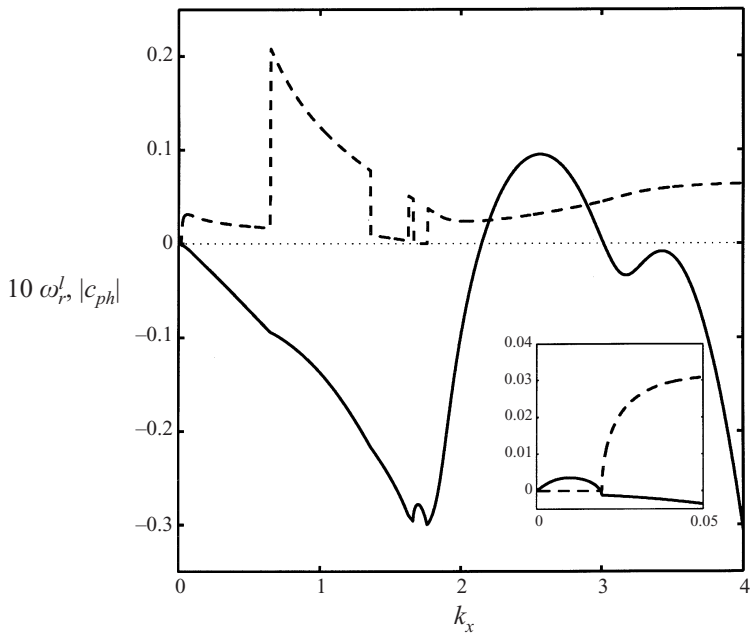

FIGURE 13. The growth rate and phase velocity of the leading mode as a function of k_x at $\overline{\nu} = 0.30$ and $H = 50$ for source walls ($e_p = 0.80$ and $e_w = 0.97$). The inset shows the variation for long waves.

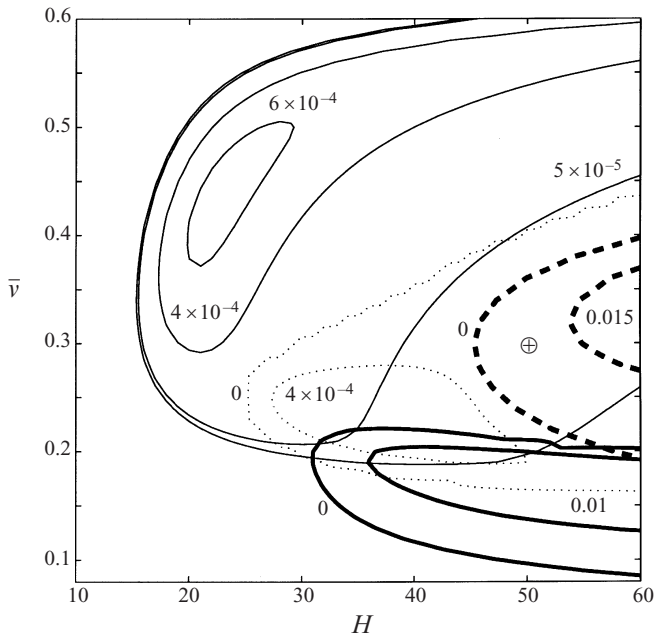

FIGURE 14. The complete stability map in the $(H, \overline{v})$-plane for the case of source walls. The thin solid lines are growth rate contours for layering modes ($k_x = 0$), the dotted lines for long-wave modes, the thick solid lines for strong stationary waves, and the thick dashed lines for travelling waves.

with change in H or $\overline{v}$. When H is small or $\overline{v}$ is large, the dominant long-wave instability occurs not at a finite wavenumber but is a layering mode, as was always the case in the adiabatic case. The modes on the second hill, which are travelling waves in figure 13, become stationary waves for small mean densities; sometimes the hill starts with stationary waves and turns into travelling waves. The third hill rises above the baseline as H increases, although the dominant mode is always the mode corresponding to the peak of the second hill. At large H even more hills of travelling waves rise above the baseline.

Contours of constant growth rate in the $(H, \overline{v})$-plane for all the modes are given in figure 14. It is significant that the dilute flow instability that we observed in the adiabatic case (figure 10) is absent here. The overall neutral stability contour in this figure originates from layering modes for $\overline{v}$ above 0.18, from long waves for a very short span of $\overline{v}$ below 0.18 and stationary waves for even lower mean densities. While the travelling wave instability does not affect the neutral stability contour, it is the fastest growing mode in most of the region where it is unstable. As in the adiabatic case, the flow is stable when either the mean density or the Couette gap is sufficiently small. It is interesting to note that the upper envelope of stationary instability appears to fall as H increases, suggesting that these modes remain stable beyond a mean solids fraction of roughly 0.22. This contrasts with the adiabatic case for which the upper envelope rises to cover dense flows as H increases (cf. figure 4).

We now pause to consider the layering instabilities in some detail and point out the differences with those for the case of adiabatic walls. Looking at the lower envelope of the region of instability to layering modes, we find that this instability occurs only for a finite range of H; the flow is stable when the Couette gap is large. This is

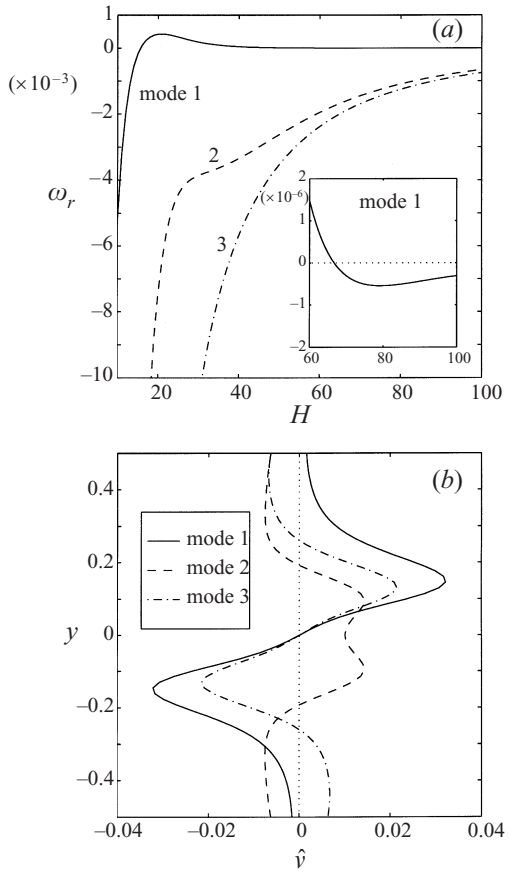

FIGURE 15. (*a*) The growth rate of first three non-oscillatory layering modes ($k_x = 0$) as a function of H. Parameter values as in figure 13. (*b*) Eigenfunctions for the solids fraction disturbance at $(H, \bar{\nu}) = (50, 0.3)$, i.e. the point $\oplus$ in figure 14.

clearly illustrated in figure 15(*a*) which shows the variation of the growth rates of the first three layering modes with H at $\bar{\nu} = 0.30$. These are non-oscillatory modes; the oscillatory modes here are always damped. The first mode becomes stable beyond $H \approx 67$, and the rest are always stable. More importantly, there are no mode crossings with increase in H, unlike in the adiabatic case where higher-order modes successively take over as the leading mode after constant intervals of H (cf. figure 5). The mode numbering in figure 15(*a*) corresponds to the number of zeros in the eigenfunctions for $\hat{v}(y)$, shown in figure 15(*b*); $\hat{v}(y)$ has one zero for the first mode, two zeros for the second mode and so on. Thus, there is clearly a one to one correspondence between these modes and the modes $n = 1,2$ etc. for the adiabatic case (5.8), showing that every layering mode of the source case can be identified with a layering mode of the adiabatic case, but the form of the eigenfunction is modulated by the boundary condition.

The eigenfunctions for the solids fraction disturbance of the dominant long wave and the dominant travelling wave modes in figure 13 are shown in figure 16. The pattern in figure 16(*a*) is stationary. There are two rows of clusters, placed symmetrically about the mid-plane at $y \approx \pm 0.15$. The pattern shown here does not reflect the true aspect of the disturbance as it has been compressed by a factor of 1256 in

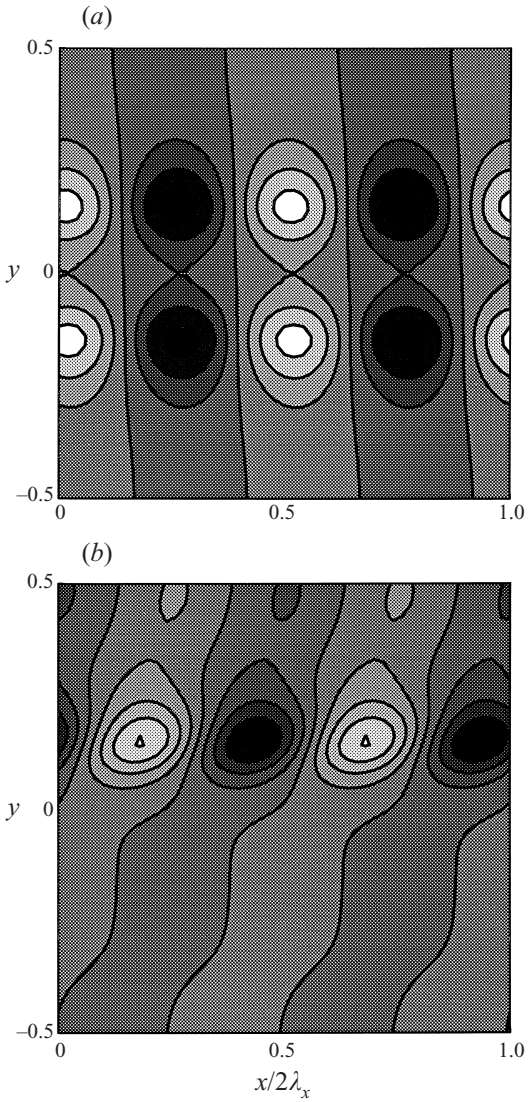

FIGURE 16. The solids fraction disturbance for (*a*) the dominant long-wave ($k_x = 0.01$) and (*b*) the dominant travelling wave ($k_x = 2.56$) instabilities in figure 13.

the x-direction. The travelling wave pattern in figure 16(*b*) propagates in the positive x-direction; there is also a backward propagating wave with the same growth rate for which the density pattern is a 180°-rotation of that given here. The phase velocity of these travelling waves is 0.03 and the base-state velocity at the centre of the clusters is roughly the same. Therefore, the clusters do convect with the local mean velocity.

That the instabilities are driven by the inelasticity of grain collisions may be ascertained by looking at the variation of ω_r^l with k_x for different values of e_p. For example, on increasing e_p to 0.9 (with other parameters as in figure 13) the travelling waves become stable and the fastest growing disturbance is a layering mode. As e_p is reduced, the dominant long-wave and travelling wave instabilities become stronger. The details of these computations are documented in Alam (1998).

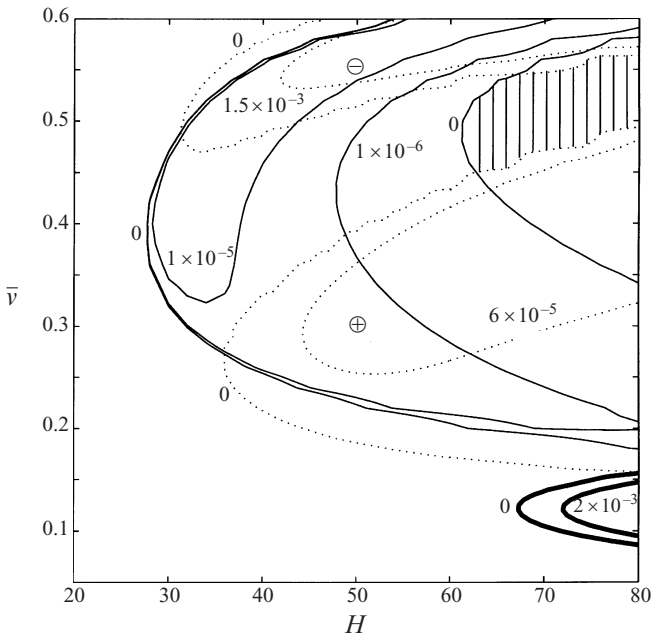

FIGURE 17. The complete stability map in the $(H, \bar{\nu})$-plane for the case of sink walls ($e_p = 0.80$ and $e_w = 0.50$). The thin solid lines are growth rate contours for layering modes, the dotted lines for long-wave modes, and the thick solid lines for strong stationary waves. The flow is stable to all perturbations in the hatched region.

7. Walls acting as energy sinks

We now consider stability for the case when the walls act as sinks of pseudo-thermal energy. We recall from § 3.1 that the base state for this case has dense non-deforming plugs near the walls, confining the shearing zone to around the symmetry axis. Here too the computational difficulty in determining eigenvalues when the plugs are dense has limited the range of H for which we have determined stability. We show below that while there are some similarities in the stability characteristics with those for adiabatic and source walls, there also are significant differences.

Figure 17 shows the stability map in the $(H, \bar{\nu})$-plane. The dilute flow instability that was present in the case of adiabatic walls is absent here. There is now a long-wave stationary instability which is dominant for dense flows and forms the upper envelope of the unstable region. The long-wave modes which are present at low-to-moderate mean density are travelling instabilities. It is evident that the growth rates in figure 17 are in general much smaller than in the source case. The strong stationary wave instability that was prominent in the adiabatic and source cases is also present here, but only at larger H. The hatched region near the top right-hand corner is stable to all disturbances.

The variation of the leading modes with k_x for the points $\oplus$ and $\ominus$ in figure 17 are shown in figure 18. The growth rate at $\ominus$ has been reduced by a factor of 20 to accommodate it in this plot. The leading mode remains stable for k_x above 0.05 at these points. In both cases, the leading mode originates from an unstable non-oscillatory layering mode, remains a stationary wave for a range of k_x, and thereafter becomes a travelling wave. The dominant modes at the points $\oplus$ and $\ominus$ in figure 17 are travelling and stationary waves, respectively.

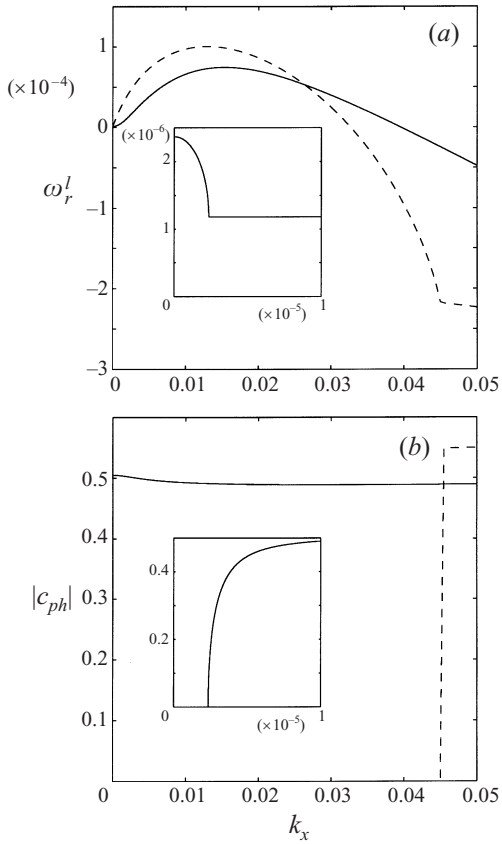

FIGURE 18. The variation of (*a*) the growth rate of the leading mode and (*b*) its phase velocity with wavenumber k_x for the points ⊕ (solid line, $\overline{v} = 0.3$, $H = 50$) and ⊖ (dashed line, $\overline{v} = 0.55$, $H = 50$) in figure 17. The inset in each panel shows the variation of the former for very small k_x.

Figure 19(*a*) shows the eigenfunction for the solids fraction for the dominant mode at the point ⊕ in figure 17, a travelling wave with phase velocity $c_{ph} \approx 0.488$. The maximum density fluctuation occurs at $y \sim 0.35$ where the base-state velocity is about 0.41. Therefore, the clusters convect slightly faster than the local mean flow. The structure of the dominant disturbance is very different when $\overline{v}$ is raised to 0.55 (the point ⊖ in figure 17), as illustrated in figure 19(*b*). The clusters are now centred on the mid-plane and the disturbance is stationary. In contrast, the dominant instability for the case of source walls at the same $\overline{v}$ and H is a layering mode with maximum density fluctuation roughly halfway from the centreline to the wall. The eigenfunctions for the strong stationary instability corresponding to the thick lines in figure 17 are quite similar to those of the adiabatic case (figure 8*a*). This is not surprising, since the base state for dilute flows is relatively insensitive to the properties of the walls.

Lastly, we consider stability when the Couette gap is large to investigate if any new qualitative features arise that were not present for the parameter range in figure 17. We show the variation of the leading mode with k_x in figure 20 for $(H, \overline{v}) = (145, 0.3)$. It required 225 collocation points to obtain eigenvalues with the desired accuracy for this parameter set. There are now three hills above the baseline of zero growth rate (this figure does not resolve the long-wave modes such as in figure 18): the first two hills are the travelling waves that are also present at a smaller H in figure 18,

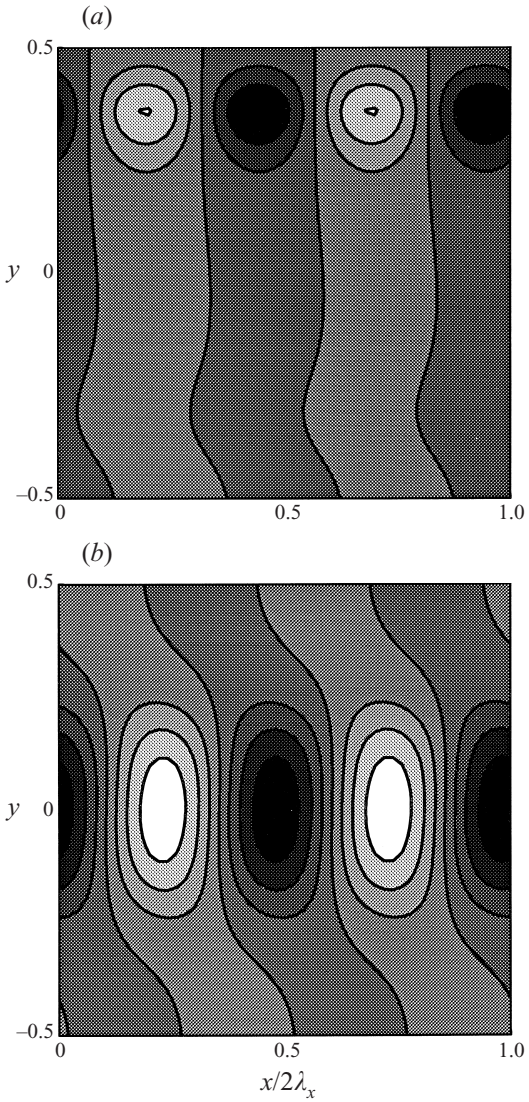

FIGURE 19. The solids fraction disturbance of the dominant modes at the points ⊕ and ⊖ in figure 17. (*a*) $\overline{\nu} = 0.30$, $H = 50$, $k_x = 0.015$; (*b*) $\overline{\nu} = 0.55$, $H = 50$, $k_x = 0.013$. The patterns must be stretched by factors of 840 and 965, respectively, in the x-direction to view their true aspect.

and the third is the strong stationary wave instability, represented by the thick solid contours in figure 17. Thus the region in the $(H,\overline{\nu})$-plane where these stationary waves are unstable grows to encompass dense flows as H increases, unlike the case of source walls for which there is an upper bound in $\overline{\nu}$ for this instability. As in the case of adiabatic walls, the dominant stationary wave originates from the first pair of oscillatory layering modes. The eigenfunctions for the solids fraction for the disturbance corresponding to the second and third peaks of figure 20 are shown in figures 21(*a*) and 21(*b*), respectively. The significant difference between the patterns in figures 21(*a*) and 19(*a*) is that the clusters in the former are more compact and lie some distance from the walls. The distance they are displaced is in fact the thickness of the dense plugs in the base state. This is also the case for the stationary wave

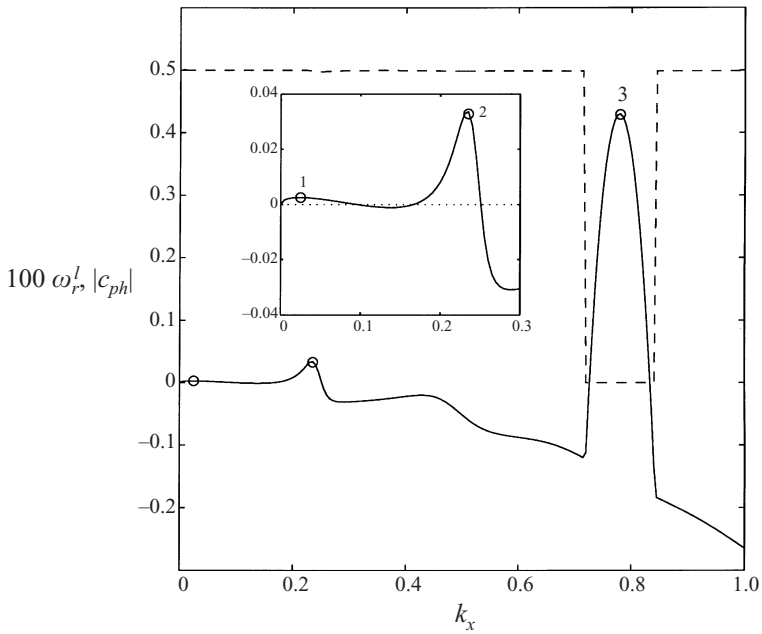

FIGURE 20. The variation of leading mode with k_x at $H = 145$, $\bar{\nu} = 0.3$ with other parameters as in figure 18. The solid and dashed lines represent the growth rate and phase velocity, respectively. Note the presence of strong stationary wave instabilities.

pattern in figure 21(*b*), which may be compared with that of the adiabatic case in figure 8(*a*); but for the compression of the clusters and their displacement from the walls, the pattern is similar to that in the adiabatic case.

8. Summary and conclusions

The linear stability of plane Couette flow of a granular material was considered, using a kinetic-theory-based model for the rheology. Our original idea of including the stress arising from grain friction was abandoned due to difficulties encountered in determining the base state; when the Couette gap is sufficiently large, there are dense slowly deforming regions and the frictional stress is indeterminate. Stability was determined for three illustrative sets of wall properties, corresponding to the walls being perfectly adiabatic, and acting as sources and sinks of fluctuational energy. For a given set of material and wall properties, stability is a function of the Couette gap H and the mean solids fraction $\bar{\nu}$. For all three cases, the flow is stable if H is sufficiently small. The flow is also stable for all H if $\bar{\nu}$ is sufficiently small, with the exception of the case of adiabatic walls when there is a low-density instability.

The dominant instability may be one of three types: (i) a slowly growing pattern of alternating layers of higher and lower density parallel to the walls (layering modes), (ii) a more complicated relatively fast growing stationary pattern with variation in the flow direction and (iii) a similar pattern travelling in the direction of mean flow which grows rapidly when the walls are adiabatic or sources of energy and relatively slowly when they are energy sinks. In the second and third types above, clusters of particles are evident. The clusters in the travelling wave instability do not necessarily convect with the local mean velocity. For the case of adiabatic walls, there is another instability at low densities; the instability pattern is that of a stationary density wave in the streamwise direction with almost no variation in the gradient direction.

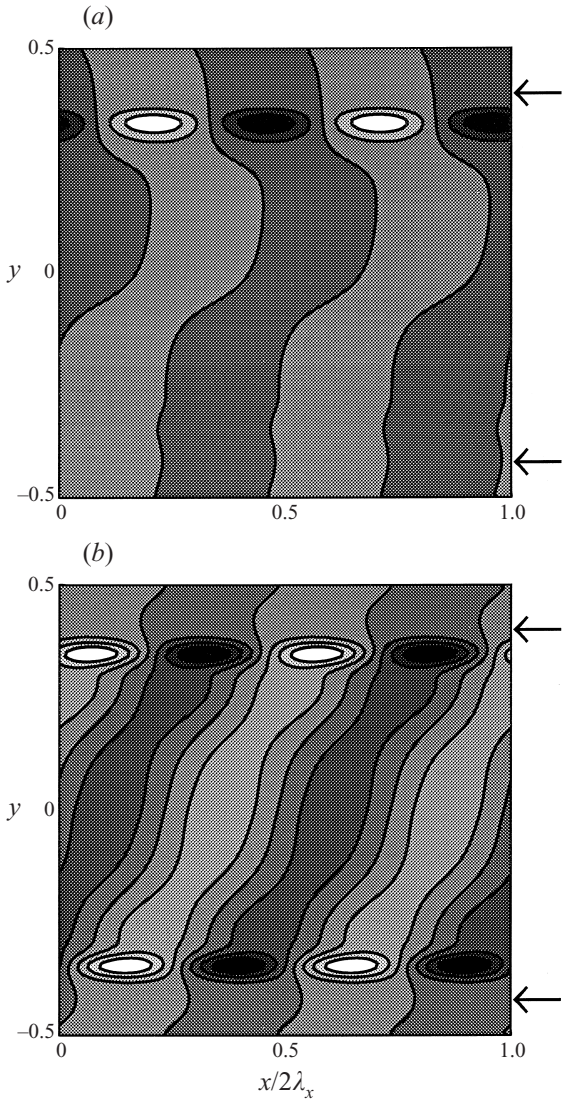

FIGURE 21. The solids fraction disturbance of the dominant modes in figure 20. Panel (*a*) is the (forward propagating) travelling instability corresponding to the second peak in the growth rate of figure 20 and panel (*b*) is the strong stationary wave instability corresponding to the third peak. The arrows in each panel indicate the locations where the base-state solids fraction is 0.649.

This investigation follows the recent paper of Wang *et al.* (1996) on the same topic. However, our findings differ significantly from theirs on the base-state solutions and consequently, on the stability characteristics when the walls act as sources or sinks of fluctuational energy. They did not observe the dense plugs that we find to be characteristic of plane Couette flow when the gap is sufficiently large. This appears to be due to inaccuracies in the numerical solution procedure adopted by them. As a result, the contours of neutral stability as well as the details of the unstable modes that we have computed substantially differ from those that they have reported. In the case of adiabatic walls, when the base state is devoid of dense plugs, Wang *et al.* appear to have missed the strong travelling wave instabilities and the dilute flow stationary instabilities (cf. § 5.1.1) that we have observed.

Instability is essentially caused by the inelasticity of grain collisions; the growth rate of all instabilities decreases as the coefficient of restitution e_p approaches unity. The compressibility of the granular medium is also an essential feature, as the primary manifestation of instability is the formation of clusters or alternating layers of high and low density. We note in this regard that in our earlier paper on the stability of unbounded shear (Alam & Nott 1997) we have demonstrated that there is no instability if the granular medium is assumed to be incompressible. The dependence of the transport properties of the medium on the grain temperature is also necessary for the observed instabilities, as it provides the coupling between the energy and momentum balances.

The properties of the bounding walls strongly determine the nature of the base states, and the onset and nature of instabilities. However, we must emphasize here that the differences in stability between the adiabatic, source and sink cases are primarily due to the differences in their base states. If, for instance, the uniform-shear base state is analysed in all three cases (it will, of course, not satisfy boundary conditions (3.5)–(3.8) for source and sink walls), the stability characteristics differ only marginally. Indeed, there are steady fully developed solutions for the adiabatic case that closely resemble the base-state solutions of the source and sink cases; these are simply steady states of the layering mode instabilities that arise from the uniform shear solution. These segregated solutions for the adiabatic case, and their corresponding solutions in the source and sink cases are analysed in a forthcoming paper by Nott *et al.* (1998). For instance, the mode corresponding to $n = 2$ of (5.8) leads to two steady solutions for each set of H and $\overline{v}$, one resembling the base state of the source case and the other resembling the base state of the sink case. Consequently, the stability characteristics of these solutions for the adiabatic case are very similar to that of the source and sink cases reported in §§ 6 and 7 of this paper.

A comment on the generality of our findings is necessary, as we have chosen one of several available constitutive models, and the question arises as to whether the results we have presented are specific to this model or whether they are of general import. The model of Lun *et al.* that we have used accounts for the perturbation from the Maxwellian velocity distribution function up to terms that are linear in the gradients of the hydrodynamic variables. Jenkins & Richman (1985) have shown that any systematic derivation that stops at linear corrections will yield identical constitutive relations. The results we have presented here are therefore general, if the gradients of the hydrodynamic fields and the inelasticity of grain collisions are small. One feature that these models do not capture is the anisotropy of the velocity distribution function, observed in computer simulations of Walton & Braun (1986), and derived in the kinetic theories of Jenkins & Richman (1988) and Sela & Goldhirsch (1998). However the analysis of Sela & Goldhirsch, which carries the expansion of the velocity distribution function up to Burnett order, clearly shows that anisotropy (and consequently normal stress differences) arises from terms of Burnett order. While it is certainly of interest to conduct a stability analysis using this higher-order model, it is a separate study in itself and we leave it to a future investigation. In this context, we note that the value 0.8 assigned to e_p in this study may perhaps not be close enough to unity to satisfy the assumption of small inelasticity in the model of Lun *et al.* (we had used it to enable direct comparison with the results of Wang *et al.*). This is however not a serious issue, as our qualitative findings apply to a range of e_p that is close enough to unity.

As noted in our earlier paper (Alam & Nott 1997), a linear stability analysis of unbounded shear predicts that the only instabilities that arise are of the layering kind. The microstructures observed by Hopkins & Louge (1991) in their simulations

of unbounded shear of smooth inelastic disks are however not of this type, but are finite sized clusters whose principal axis is inclined from the flow direction. While the use of periodic boundaries in simulations constrains the wavelengths of disturbances to be less than the size of the periodic cell, the singular limit of infinite wavelength (no variation in the streamwise direction) ought to be captured in simulations. Indeed, structures remarkably similar to layering modes have been reported by Tan (1995) in simulations of plane Couette flow of inelastic disks (with periodic boundaries in the flow direction). Possible reasons for why layering structures were absent in the simulations of Hopkins & Louge are nonlinear or finite-amplitude effects and unavoidable numerical error, but we are unable to speculate further.

It is well known that when dense granular materials are sheared, often deformation occurs only in thin shear layers while most of the material remains undeformed (see, for example, Schoefield & Wroth 1958, p. 223). It is interesting that a model which is expected to hold only in the regime of rapid flow predicts this type of layering instability with alternating layers of high and low density. Even the solutions for the base state of steady fully developed plane Couette flow indicate that the flow domain is divided into shearing and dense non-shearing (plug) zones, except in the singular case of there being no-slip and no energy flux at the walls. This suggests that even when the mean density is well within that of loose random packing (i.e. when grains are not in sustained contact with their neighbours), there are regions in the flowing material where the density is high enough (and the deformation slow enough) that the effects of grain friction may not be ignored. Although this study may not be of immediate consequence to practical problems in the shear of granular materials where gravitational compaction and grain friction may be important, we hope that it is a step in the right direction. In this regard, it would be useful to extend this analysis by including the effects of gravity and friction.

We wish to thank Professor Vijay H. Arakeri for his encouragement and suggestions during the course of this work. The paper was written when M.A. was supported by a Project Assistantship by the Jawaharlal Nehru Centre for Advanced Scientific Research, Bangalore.

Appendix. Linearized stability equations and boundary conditions

The linearized equations for the disturbance variables v', u', v', and T' are

$$\frac{\partial v'}{\partial t} + u^0\frac{\partial v'}{\partial x} + v^0\frac{\partial u'}{\partial x} \quad + \left(v_y^0 + v^0\frac{\partial}{\partial y}\right)v' = 0, \tag{A 1}$$

$$\begin{aligned} v^0H^2\left[\frac{\partial u'}{\partial t} + u^0\frac{\partial u'}{\partial x} + u_y^0 v'\right] = {} & \left[-p_v^0\frac{\partial}{\partial x} + u_y^0\left(\mu_{vv}^0 v_y^0 + \mu_{vT}^0 T_y^0\right) + u_{yy}^0\mu_v^0 + u_y^0\mu_v^0\frac{\partial}{\partial y}\right]v' \\ & + \left[\left(2\mu^0 + \lambda^0\right)\frac{\partial^2}{\partial x^2} + \mu_y^0\frac{\partial}{\partial y} + \mu^0\frac{\partial^2}{\partial y^2}\right]u' \\ & + \left[\mu_y^0\frac{\partial}{\partial x} + \left(\mu^0 + \lambda^0\right)\frac{\partial^2}{\partial x\partial y}\right]v' \\ & + \left[-p_T^0\frac{\partial}{\partial x} + u_y^0\left(\mu_{Tv}^0 v_y^0 + \mu_{TT}^0 T_y^0\right) + u_{yy}^0\mu_T^0 + u_y^0\mu_T^0\frac{\partial}{\partial y}\right]T', \end{aligned} \tag{A 2}$$

$$v^0 H^2\left[\frac{\partial v'}{\partial t}+u^0\frac{\partial v'}{\partial x}\right]=\left[u^0_y\mu^0_v\frac{\partial}{\partial x}-\left(p^0_{vv}v^0_y+p^0_{vT}T^0_y\right)-p^0_v\frac{\partial}{\partial y}\right]v'$$
$$+\left[\lambda^0_y\frac{\partial}{\partial x}+\left(\mu^0+\lambda^0\right)\frac{\partial^2}{\partial x\partial y}\right]u'$$
$$+\left[\mu^0\frac{\partial^2}{\partial x^2}+\left(2\mu^0_y+\lambda^0_y\right)\frac{\partial}{\partial y}+\left(2\mu^0+\lambda^0\right)\frac{\partial^2}{\partial y^2}\right]v'$$
$$+\left[u^0_y\mu^0_T\frac{\partial}{\partial x}-\left(p^0_{Tv}v^0_y+p^0_{TT}T^0_y\right)-p^0_T\frac{\partial}{\partial y}\right]T', \qquad (A\,3)$$

$$\tfrac{3}{2}v^0\left[\frac{\partial T'}{\partial t}+u^0\frac{\partial T'}{\partial x}+T^0_y v'\right]=\frac{1}{H^2}\left[\kappa^0_h\frac{\partial^2}{\partial x^2}+\left(T^0_{yy}\kappa^0_v+T^0_y\kappa^0_{vy}\right)\right.$$
$$\left.+\left(v^0_{yy}\kappa^0_{hv}+v^0_y\kappa^0_{hvy}\right)+H^2\left(\mu^0_v u^{0^2}_y-\mathscr{D}^0_v\right)\right.$$
$$\left.+\left(\kappa^0_{hy}+v^0_y\kappa^0_{hv}+T^0_y\kappa^0_v\right)\frac{\partial}{\partial y}+\kappa^0_h\frac{\partial^2}{\partial y^2}\right]v'$$
$$+\left[-p^0\frac{\partial}{\partial x}+2u^0_y\mu^0\frac{\partial}{\partial y}\right]u'+\left[2u^0_y\mu^0\frac{\partial}{\partial x}-p^0\frac{\partial}{\partial y}\right]v'$$
$$+\frac{1}{H^2}\left[\kappa^0\frac{\partial^2}{\partial x^2}+\left(T^0_{yy}\kappa^0_T+T^0_y\kappa^0_{Ty}\right)\right.$$
$$\left.+\left(v^0_{yy}\kappa^0_{hT}+v^0_y\kappa^0_{hTy}\right)+H^2\left(\mu^0_T u^{0^2}_y-\mathscr{D}^0_T\right)\right.$$
$$\left.+\left(\kappa^0_y+T^0_y\kappa^0_T+v^0_y\kappa^0_{hT}\right)\frac{\partial}{\partial y}+\kappa^0\frac{\partial^2}{\partial y^2}\right]T'. \qquad (A\,4)$$

Here the subscripts v, T and y indicate partial derivatives and the superscript 0 stands for quantities evaluated at the base state conditions.

The boundary conditions (2.14)–(2.15) are linearized to yield

$$\left.\begin{array}{c}\left[H\phi' f^0_{7v}\left(u^0-1/2\right)\right]v'+\left[H\phi' f^0_7+\dfrac{\partial}{\partial y}\right]u'=0,\\ v'=0,\\ \left[f^0_{6v}\left(\tfrac{1}{3}H^3\phi'\left(u^0-1/2\right)^2-\tfrac{1}{2}H\left(1-e_w^2\right)T^0\right)\right.\\ \left.-T^0\left(\dfrac{f^0_{4hv}}{f^0_4}-f^0_{4h}\dfrac{f^0_{4v}}{f^{0^2}_4}\right)v^0_y-T^0\dfrac{f^0_{4h}}{f^0_4}\dfrac{\partial}{\partial y}\right]v'\\ +\left[\tfrac{2}{3}H^3\phi'\left(u^0-1/2\right)f^0_6\right]u'+\left[-\tfrac{1}{2}H\left(1-e_w^2\right)f^0_6-\dfrac{f^0_{4h}}{f^0_4}v^0_y-\dfrac{\partial}{\partial y}\right]T' \;=\; 0,\end{array}\right\} \qquad (A\,5)$$

at $y = 1/2$ and

$$\left.\begin{aligned}
\left[H\phi' f_{7v}^0 \left(u^0 + 1/2\right)\right] v' + \left[H\phi' f_7^0 - \frac{\partial}{\partial y}\right] u' &= 0, \\
v' &= 0, \\
\left[f_{6v}^0 \left(\tfrac{1}{3}H^3\phi' \left(u^0 + 1/2\right)^2 - \tfrac{1}{2}H\left(1 - e_w^2\right) T^0\right)\right. & \\
\left. + T^0 \left(\frac{f_{4hv}^0}{f_4^0} - f_{4h}^0 \frac{f_{4v}^0}{f_4^{0\,2}}\right) v_y^0 + T^0 \frac{f_{4h}^0}{f_4^0} \frac{\partial}{\partial y}\right] v' & \\
+ \left[\tfrac{2}{3}H^3\phi' \left(u^0 + 1/2\right) f_6^0\right] u' + \left[-\tfrac{1}{2}H\left(1 - e_w^2\right) f_6^0 + \frac{f_{4h}^0}{f_4^0} v_y^0 + \frac{\partial}{\partial y}\right] T' &= 0,
\end{aligned}\right\} \quad \text{(A 6)}$$

at $y = -1/2$. The condition $v' = 0$ is a statement of impenetrability of the walls.

REFERENCES

Alam, M. 1998 Stability of unbounded and bounded granular shear flows. PhD thesis, Indian Institute of Science, Bangalore.

Alam, M. & Nott, P. R. 1997 The influence of friction on the stability of unbounded granular shear flow. *J. Fluid Mech.* **343**, 267–301.

Babić, M. 1993 On the stability of rapid granular flows. *J. Fluid Mech.* **254**, 127–150.

Canuto, C., Hussaini, M. Y., Quarteroni, A. & Zang, T. A. 1988 *Spectral Methods in Fluid Dynamics*. Springer.

Craik, A. D. D. 1985 *Wave Interactions and Fluid Flows*. Cambridge University Press.

Drazin, P. G. & Reid, W. H. 1981 *Hydrodynamic Stability*. Cambridge University Press.

Duck, P. W., Erlebacher, G. & Hussaini, M. Y. 1994 On the linear stability of compressible plane Couette flow. *J. Fluid Mech.* **258**, 131–165.

Gallagher, A. P. & Mercer, A. McD. 1962 On the behaviour of small disturbances in plane Couette flow. *J. Fluid Mech.* **13**, 91–100.

Goldhirsch, I., Tan, M-L. & Zanetti, G. 1993 A molecular dynamical study of granular fluids **I**: the unforced granular gas in two dimensions. *J. Sci. Comput.* **8**, 1–40.

Golub, G. H. & van-Loan, C. F. 1989 *Matrix Computations*. The Johns Hopkins University Press, Baltimore.

Gustavsson, L. H. & Hultgren, L. S. 1980 A resonance mechanism in plane Couette flow. *J. Fluid Mech.* **98**, 149–159.

Hopkins, M. A. & Louge, M. Y. 1991 Inelastic microstructure in rapid granular flows of smooth disks. *Phys. Fluids* A **3**, 47–57.

Hui, K., Haff, P. K., Ungar, J. E. & Jackson, R. 1984 Boundary conditions for high-shear grain flows. *J. Fluid Mech.* **145**, 223–233.

Jenkins, J. T. 1992 Boundary conditions for rapid granular flow: flat, frictional walls. *Trans. ASME: J. Appl. Mech.* **59**, 120–127.

Jenkins, J. T. & Richman, M. W. 1985 Grad's 13-moment system for a dense gas of inelastic spheres. *Arch. Rat. Mech. Anal.* **87**, 355–377.

Jenkins, J. T. & Richman, M. W. 1986 Boundary conditions for plane flows of smooth, nearly elastic, circular disks. *J. Fluid Mech.* **171**, 53–69.

Jenkins, J. T. & Richman, M. W. 1988 Plane simple shear of smooth inelastic circular disks: the anisotropy of the second moment in the dilute and dense limit. *J. Fluid Mech.* **192**, 313–328.

Jenkins, J. T. & Savage, S. B. 1983 A theory for the rapid flow of identical, smooth, nearly elastic, circular particles. *J. Fluid Mech.* **130**, 187–202.

Johnson, P. C. & Jackson, R. 1987 Frictional-collisional constitutive relations for granular materials, with application to plane shearing. *J. Fluid Mech.* **176**, 67–93.

Lun, C. K., Savage, S. B., Jeffrey, D. J. & Chepurniy, N 1984 Kinetic theories for granular flow: inelastic particles in Couette flow and slightly inelastic particles in a general flow field. *J. Fluid Mech.* **140**, 223–256.

Malik, M. R. 1990 Numerical methods for hypersonic boundary layer stability. *J. Comput. Phys.* **86**, 376–413.

Miller, T. M., O'Hern, C. & Behringer, R. P. 1996 Stress fluctuations for continuously sheared granular materials. *Phys. Rev. Lett.* **77**, 3110–3113.

Mohan, L. S., Nott, P. R. & Rao, K. K. 1997 Fully developed flow of coarse granular materials through a vertical channel. *Chem. Engng Sci.* **52**, 913–934.

Nott, P. R., Alam, M., Agrawal, K., Jackson, R. & Sundaresan, S. 1998 The effect of boundaries on plane Couette flow of granular materials: a bifurcation analysis. *J. Fluid Mech.* (submitted).

Richman, M. W. 1988 Boundary conditions based upon a modified Maxwellian velocity distribution for flows of identical, smooth, nearly elastic spheres. *Acta Mechanica* **75**, 227–240.

Savage, S. B. 1992*a* Numerical simulations of Couette flow of granular materials: spatio-temporal coherence and 1/f noise. In *Physics of Granular Media* (ed. D. Bideau & J. Dodds), pp. 343–362. New York: Nova Science.

Savage, S. B. 1992*b* Instability of unbounded uniform granular shear flow. *J. Fluid Mech.* **241**, 109–123.

Schmid, P. J. & Kytömaa, H. K. 1994 Transient and asymptotic stability of granular shear flow. *J. Fluid Mech.* **264**, 255–275.

Schoefield, A. N. & Wroth, C. P. 1958 *Critical State Soil Mechanics.* McGraw-Hill.

Sela, N. & Goldhirsch, I. 1998 Hydrodynamic equations for rapid flows of smooth inelastic spheres, to Burnett order. *J. Fluid Mech.* **361**, 41–74.

Tan, M. L. 1995 Microstructures and Macrostructures in rapid granular flows. PhD Dissertation, Princeton University.

Walton, O. R. & Braun, R. L. 1986 Viscosity, granular temperature, and stress calculations for shearing assemblies of inelastic, frictional disks. *J. Rheol.* **30**, 949–980.

Wang, C-H., Jackson, R. & Sundaresan, S. 1996 Stability of bounded rapid shear flows of a granular material. *J. Fluid Mech.* **308**, 31–62.